

## FEATURE ARTICLE

## Dynamics of Clusters Initiated by Photon and Surface Impact

Akira Terasaki<sup>†</sup>*Cluster Research Laboratory, Toyota Technological Institute, in East Tokyo Laboratory, Genesis Research Institute, Inc., 717-86 Futamata, Ichikawa, Chiba 272-0001, Japan**Received: January 3, 2007; In Final Form: April 14, 2007*

Clusters of atoms/molecules show dynamics characteristic of the method of excitation. Two contrasted processes are discussed: (1) electronic excitation via single-photon absorption and (2) impulsive excitation of nuclear motions by surface impact. Process 1 is exemplified by photodissociation dynamics of size-selected metal cluster ions. The electronic energy is converted most likely to vibrational energy of internal modes; dissociation follows via statistical mechanism to produce energetically favored fragments. Exceptionally, a silver cluster ion,  $\text{Ag}_4^+$ , is shown to undergo nonstatistical dissociation along the potential-energy surface of the excited state. Energy partitioning to translational and vibrational modes of fragments is analyzed as well as bond dissociation energies. Furthermore, the spectrum of the photodissociation yield provides electronic and geometrical structures of a cluster with the aid of ab initio calculations; manganese,  $\text{Mn}_N^+$ , and chromium,  $\text{Cr}_N^+$ , cluster ions are discussed, where the importance of magnetic interactions is manifested. On the other hand, momentum transfer upon surface impact plays a role in process 2. An impulsive mechanical force triggers extraordinary chemical processes distinct from those initiated by atomic collision as well as photoexcitation. Experiments on aluminum,  $\text{Al}_N^-$ , silicon,  $\text{Si}_N^-$ , and solvated,  $\text{I}_2^-(\text{CO}_2)_N$ , cluster anions provide evidence for reactions proceeding under extremely high temperatures, such as pickup of surface atoms, annealing of products, and mechanical splitting of chemical bonds. In addition, a model experiment to visualize and time-resolve the cluster impact process is performed by using a micrometer-sized liquid droplet. Multiphoton absorption initiates superheating of the droplet surface followed by a shock wave and disintegration into a number of small fragments (shattering). These studies further reveal how the nature of chemical bonds influences the dynamics of clusters.

## I. Introduction

Atomic and molecular clusters offer a unique opportunity to elucidate how the physical and chemical properties of matter emerge, as atoms and molecules associate together one by one. Although the properties of solids and liquids may be extrapolated to those of small fragments by scaling down, this simple prediction is different from the reality in nanometer-sized particles as first pointed out in the framework of the quantum size effect by Kubo.<sup>1</sup> In particular, the properties change irregularly in a nonscalable manner with the number of constituent atoms or molecules (size) in the cluster regime. This size specificity is the most distinct feature of clusters, which is manifested most clearly in free clusters isolated in the gas phase. The specific size of a cluster may be referred to as a magic number, when it is distinguishable from those of neighboring sizes in properties such as abundance, reactivity, ionization potential, electron affinity, bond dissociation energy, etc. These properties have been studied extensively and have been reviewed in many articles.<sup>2–15</sup> The primary factor determining properties of a cluster is its electronic and geometrical structures, which are investigated by various experiments including laser spectroscopy, atomic collisions, and surface impact. Because the

experiments observe reactions of clusters following electronic and/or vibrational excitation, studies of “dynamics” as well as “structures” are important for elucidation of cluster properties. Here the “dynamics” refers to any energy-redistribution processes following excitation, which include dissociation and formation of chemical bonds, nuclear motions on a potential-energy surface, vibration, structure deformation, isomerization, phase transition, electronic-to-vibrational energy transfer, vibronic coupling, fluorescence, etc.

Clusters are distinguished from molecules in the following features: A molecule consists of atoms bound by rather rigid and directional chemical bonds, most typically covalent bonds, to form a stable group of atoms held together in a definite arrangement, which may be called a “closed” structure. A cluster, on the other hand, has an “open” structure, which can bind more and more atoms by the same type of interaction to grow larger without a size limitation. In contrast to the well-defined geometrical structures of molecules, a cluster often has a floppy structure with many structure isomers nearly degenerate in energy and thus possesses large entropy. These features in the structure influence the dynamics of clusters as well; for example, strong vibronic coupling, which often causes quenching of fluorescence due to rapid conversion of electronic energy to vibrational energies of internal modes (thermal energy) in

<sup>†</sup> E-mail: terasaki@clusterlab.jp.



**Akira Terasaki** received his B.Sc., M.Sc., and D.Sc. in Physics from the University of Tokyo in 1986, 1988, and 1992, respectively. He then became a research associate in Department of Chemistry at the University of Tokyo. In 1997 he moved to Toyota Technological Institute, where he is currently a professor of the Cluster Research Laboratory. His research interests focus on the electronic structures and dynamics of size-selected clusters in the gas phase and on solid surfaces by means of laser spectroscopy, mass spectrometry, and ion beams and traps as major techniques in experiments.

the ground state, and phase transitions due to entropy as manifested in surface-impact processes. The dynamics of clusters are thus essentially important and should be distinguished from that of molecules.

Excitation of clusters is often initiated either by photons or by collisions. Single-photon excitation of an electronic transition of a metal cluster in the visible range deposits an amount of energy comparable to a bond dissociation energy. The electronic energy is transferred, in most cases, to thermal energy; the cluster dissociates then in a statistical manner via an energetically favored pathway, i.e., according to energetics. Therefore, these processes have been used, for example, for determination of binding energies by the measurement of a unimolecular dissociation rate.<sup>16–19</sup> However, we also find exceptional cases, where dissociation occurs in a nonstatistical manner; i.e., the process is governed by dynamics on the potential-energy surface rather than energetics. This indicates a weak coupling between the electronic state and vibrational modes of the system, which might be related to the origin of fluorescence found recently for silver clusters in a rare-gas matrix.<sup>20–23</sup> The reason for this long lifetime of the excited electronic state in small and cold clusters is currently an open question.

On the other hand, an atomic collision transfers its translational energy to a target cluster via vibrational excitation. This process is useful for the measurement of binding energies by analysis of a threshold energy for dissociation (collision-induced dissociation, CID);<sup>24</sup> the vibrational energy of the local mode excited is rapidly redistributed to thermal energy, which leads the cluster to dissociate statistically. Collisional excitation induces a collective motion of constituent atoms as well depending on the excitation energy. For example, a breathing motion of argon clusters has been predicted by molecular-dynamics (MD) simulations<sup>25,26</sup> and observed indeed by experiments<sup>27,28</sup> using scattering of a He atom beam; the low-energy collision of He excites the low-frequency collective vibration efficiently. A sodium cluster ion,  $\text{Na}_9^+$ , in collision with a Ne atom has been found to release  $\text{Na}_2$  preferentially over Na as a result of a large-amplitude motion excited collectively, which causes significant structure deformation of a cluster; the preferential formation of  $\text{Na}_2$  is explained by selective dynamics to formation of a pair of valence electrons due to the large deformation<sup>29,30</sup> rather than by a statistical model.<sup>31</sup>

An extension along these lines is the cluster impact on a solid surface, where dynamics dominates the reaction processes even more significantly. The surface impact exerts an impulsive

mechanical force on the cluster and initiates a concerted motion of constituent atoms as a result of momentum transfer to all the atoms synchronously at the same time. At the instant of impact, the translational energy of the impinging cluster creates a local environment at an extremely high temperature above 1000 K, because of the energies of all the constituents focus on a limited area of the surface. Excitation to such a “super-high” temperature is followed by dynamical processes such as site-specific bond splitting, shock-wave generation, and fragmentation of a cluster into individual atoms or molecules (shattering). Advances of this field have recently been reviewed by Yasumatsu and Kondow.<sup>32</sup> One of the interests in these processes from a chemical point of view is the activation of four-center reactions, as proposed by Levine and co-workers based on MD simulations;<sup>33</sup> for example,  $\text{N}_2$  and  $\text{O}_2$  solvated with  $\text{Ne}_{125}$  is a cluster effective in producing NO molecules, where the solvent Ne atoms impose a geometrical constraint to the reactants, deposit energy efficiently via multiple collisions, and take away the excess thermal energy to stabilize the product. These features specific to the surface-impact process are opening a new field, namely, cluster-impact chemistry. However, experimental verification is needed to materialize these ideas predicted by computational studies.

In this Feature Article we focus on the two most contrasted processes, namely, electronic excitation by a single photon and vibrational excitation by impact on a surface, to describe the dynamics of clusters that are dependent on the method of excitation. These dynamical processes are in turn shown to provide detailed information about the properties of clusters including geometric and electronic structures, mechanical properties, magnetism, and reactivities, which are closely correlated with the nature of the chemical bond between constituent atoms and molecules.

The present Feature Article is organized as follows: First, electronic excitation by single-photon absorption is presented, where the focus is placed on photodissociation. The dissociation dynamics of a silver cluster ion,  $\text{Ag}_4^+$ , and its electronic spectrum obtained as the photon-energy dependence of dissociation cross sections (photodissociation action spectrum) are discussed in connection with the electronic and geometrical structures predicted by ab initio calculations. Bond dissociation energies determined from the photodissociation threshold are given for manganese cluster ions,  $\text{Mn}_N^+$ . It is further demonstrated that the electronic spectra provide evidence for novel magnetic properties of  $\text{Mn}_{2,3}^+$  and  $\text{Cr}_3^+$ . Second, collisional excitation is discussed. In particular, surface-impact processes provide insight into a number of energy-redistribution processes, including creation of chemical environments at a super-high temperature, site-specific bond splitting, and shattering into individual molecules, as demonstrated by aluminum,  $\text{Al}_N^-$ , silicon,  $\text{Si}_N^-$ , and solvated,  $\text{I}_2^-(\text{CO}_2)_N$ , cluster anions. Third, the surface impact of a cluster is modeled by a micrometer-sized liquid droplet excited by multiphoton absorption (MPA) at the surface. This experiment visualizes and time-resolves the dynamical processes such as shattering and shock waves predicted by MD simulations of cluster–surface impact processes. And, finally, these findings are summarized to show plausible future directions for chemistry of clusters.

## II. Single-Photon Electronic Excitation

**II.1. Dynamics Following Photoexcitation.** Single-photon excitation induces a transition of a bound electron either to an outer bound orbital or even to a continuum state no longer bound. As the excitation energy increases, (1) predissociation

starts above the bond dissociation energy, (2) direct dissociation comes into a competing channel if the excited state has a repulsive nature, (3) photodetachment starts above the adiabatic ionization/detachment energy via thermionic emission,<sup>34</sup> which competes with dissociation processes, and (4) photoionization/photodetachment dominates above the vertical ionization/detachment energy. Electronic excitation above the dissociation threshold thus initiates photochemistry including photodissociation, photoionization, and photodetachment. These processes in metal clusters and their properties derived from the dynamics are discussed in this section.

Excited states below the dissociation threshold, on the other hand, may be detected by resonance-enhanced two-photon ionization (R2PI)<sup>35,36</sup> or by laser-induced fluorescence (LIF).<sup>37–39</sup> However, ionization and fluorescence compete with nonradiative relaxation processes because an electronic energy is readily converted to thermal energy in metal clusters through strong vibronic coupling.<sup>36,40,41</sup> In fact, fluorescence has not been observed from free metal clusters with sizes  $N > 3$ . Emissivity of metal clusters is of current interest; fluorescence has recently been reported for  $\text{Ag}_N$  ( $N = 3, 4, 8, \text{ and } 9$ ) in an argon matrix.<sup>20–23</sup>

**II.1.1. Photodetachment.** Negatively charged clusters are often used for size-selected studies of kinetics of an electron liberated. As photodetachment is a vertical excitation process, it occurs in a time scale less than a femtosecond. The photon energy is converted to (1) the energy to remove an electron adiabatically (adiabatic detachment energy, ADE), (2) the internal (electronic and vibrational) energy of the cluster in the final neutral state, and (3) the kinetic energy of the electron. The energy (1) + (2) is the vertical detachment energy (VDE) obtained by the measurement of kinetic energy of the detached electron. The anion photoelectron spectroscopy (PES) provides electronic structures of mass-selected clusters.<sup>42,43</sup>

Dynamics of constituent atoms is initiated as well because the resulting neutral cluster has an internal energy; its equilibrium structure is often different from that of the anion. This dynamics is probed by the NeNePo (negative-neutral-positive) scheme; a negatively charged cluster is photodetached by a femtosecond pulse and the neutral is further ionized to a cation by a time-delayed probe pulse. It has been demonstrated first for  $\text{Ag}_3^-$ , which has a linear geometry. Due to the triangular equilibrium form of  $\text{Ag}_3$ , the neutral cluster prepared upon photodetachment starts a bending motion, which is discernible in the time-resolved signal of  $\text{Ag}_3^+$  because the ionization cross section is sensitive to the structure of  $\text{Ag}_3$ .<sup>44</sup>

**II.1.2. Photodissociation.** The photodissociation is characterized by two ways, namely, direct dissociation vs predissociation and statistical vs nonstatistical. Direct dissociation proceeds in a short (picosecond or less) time scale along a repulsive potential-energy surface in the excited electronic state (nonstatistical mechanism). Predissociation happens in a longer time scale; it occurs via a statistical mechanism after the electronic energy is converted to the ground-state thermal energy, whereas it is governed by the potential-energy surface (nonstatistical) when dissociation occurs before the thermal process.

The dissociation mechanisms are distinguished from each other by the following measurements: (1) Dissociation rates: <sup>16–19</sup> in direct dissociation, the lifetime of the excited state is short, which is comparable to the period of a characteristic vibrational mode. In predissociation, on the other hand, the lifetime depends on the excess energy and is even in the millisecond range near the dissociation threshold. (2) Kinetic-energy-release (KER):<sup>45,46</sup> photofragments in direct dissociation often possess kinetic energies higher than those produced by

statistical mechanisms. (3) Fragment-size distribution: energetically favorable fragments are produced in statistical processes, e.g., a series of sizes as a result of release of constituent atoms one-by-one (sequential evaporation). The dissociation channel is often connected to a particular size in nonstatistical processes, as demonstrated in section II.3.1 for a silver tetramer ion,  $\text{Ag}_4^+$ , producing  $\text{Ag}_2^+$  selectively.

The lifetime of the predissociating state should be taken into account when a dissociation energy is estimated from the threshold energy of photodissociation, because it could be even longer than the experimental time scale. A long lifetime causes underestimation of photodissociation cross sections as well. The lifetime effect becomes remarkable as the cluster size increases, as described in Supporting Information S1.

**II.2. Experimental Techniques for Obtaining Electronic Spectra from Photoexcitation Dynamics.** By using the above dynamics, electronic spectra are obtained for size-selected clusters by experimental techniques having high sensitivity. The spectrum is essential for elucidating physical and chemical properties of clusters including stability, structures, energetics, and reactivity, which are of primary interest from materials points of view.

**II.2.1. Photoelectron Spectroscopy.** Kinetic energies of photoelectrons are measured by a hemispherical electron analyzer,<sup>47,48</sup> a time-of-flight (TOF) technique,<sup>42,43,49,50</sup> or more recently a velocity imaging technique.<sup>51</sup> Negatively charged clusters are used for mass-selection (anion PES). We have started PES of transition-metal clusters,  $\text{Co}_N^-$  and  $\text{V}_N^-$ ,<sup>50,52</sup> and developed a method to analyze the spectra by spin-polarized discrete-variational  $X\alpha$  (DV- $X\alpha$ ) calculations.<sup>53–58</sup> Although ab initio calculations of photoelectron spectra had been limited to alkali- and noble-metal clusters,<sup>59,60</sup> our study initiated those for transition-metal clusters and has been followed by many advanced studies.<sup>11,61–65</sup>

We refer to just one example; dichromium-oxide cluster anions,  $\text{Cr}_2\text{O}_N^-$  ( $N = 1–3$ ).<sup>66,67</sup> The analysis of the photoelectron spectra revealed that the spin coupling between Cr atoms is ferromagnetic, in contrast to the antiferromagnetic  $\text{Cr}_2^-$ ; the oxygen atom bridging the Cr atoms mediates the ferromagnetic coupling in a manner similar to the superexchange interaction in the solid state. This finding evidenced that the magnetic properties can be controlled by chemical reactions, as had been predicted by theoretical studies.<sup>68–70</sup>

**II.2.2. Photodissociation Spectroscopy.** A photodissociation action spectrum provides an optical absorption spectrum on the assumption that all the photoabsorbed clusters dissociate within the experimental time scale. Therefore, excited states below the dissociation threshold have no chance to be detected. Even above the threshold, a finite lifetime of the excited state may prevent the cluster from dissociation before detection as discussed in Supporting Information S1. As the bond dissociation energy ranges from 2 to 3 eV for most of the metal clusters, it is difficult to obtain a spectrum in the infrared (IR) and even in the visible region. One method to overcome this problem is the use of rare-gas complex,  $\text{M}_N\text{Rg}$ , where M represents a metal element and Rg is a rare-gas atom. The rare-gas atom readily dissociates from the metal cluster,  $\text{M}_N$ , of interest, because it is bound very weakly (dissociation energy  $< 0.1$  eV). Thus the dissociation of Rg informs us of photoabsorption of  $\text{M}_N$  even in the mid-IR region (a rare-gas labeling technique).<sup>41,71–75</sup> It is known that Rg does not significantly perturb the electronic structure of  $\text{M}_N$  except for several cases.<sup>76</sup>

The measurement of a photodissociation action spectrum is performed either by beam-depletion measurement<sup>36,77,78</sup> or by

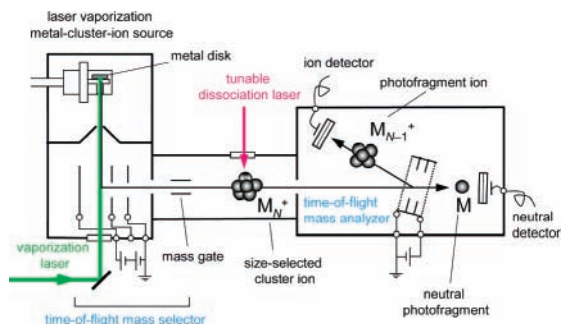


**Figure 1.** Experimental setup for photodissociation spectroscopy of cluster ions based on a photofragment-detection scheme by a tandem TOF mass spectrometer.

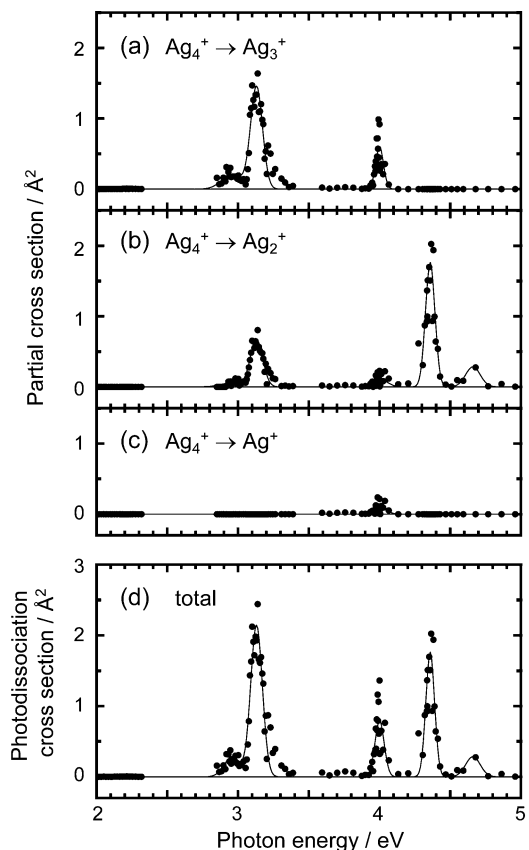
mass-analyzed photofragment detection.<sup>40</sup> In the former, the decrease in the cluster-beam intensity is observed; dissociated clusters are deflected out of the trajectory due to momentum change. Although it has been applied to measure photodissociation cross sections, it does not provide details of the dynamics because photofragments are not identified. On the other hand, the latter provides the size distribution of the fragments as well as KER for discussion of the dissociation dynamics.

Figure 1 shows our experimental setup for photodissociation spectroscopy based on photofragment detection by a tandem TOF mass spectrometer.<sup>74,79,80</sup> Briefly, metal cluster ions,  $M_N^+$ , are generated by the laser-vaporization technique<sup>37,81</sup> by using the second harmonics of a Nd:YAG laser. For the rare-gas labeling technique, about 10 vol % of an Ar gas is mixed with a buffer He gas to produce a complex,  $M_NAr^+$ . The ions produced are extracted by a pulsed electric field into a TOF spectrometer. Mass selected cluster ions are irradiated with a tunable laser pulse. Photofragment ions are mass-analyzed by the secondary TOF equipped with a reflectron. The yield of photofragment ions are recorded as the wavelength of the dissociation laser is varied. Neutral fragments are detected optionally as well behind the reflectron to obtain KER from the TOF profiles.

The advantage of the rare-gas labeling technique is exemplified by vanadium cluster ion–argon atom complexes,  $V_N^+Ar$  ( $N = 3–10$ ); photodissociation action spectra were measured in the photon-energy range between 0.6 and 3 eV. Release of Ar atom was the only dissociation channel observed because the bond dissociation energy of  $V_N^+$  is higher than 3 eV;<sup>82</sup> i.e., the spectra cannot be measured without the Ar atom. The spectra were analyzed by ab initio calculations; geometry optimization followed by calculations of transition energies and oscillator strengths.<sup>79,83–85</sup> A similar experiment has been performed for  $V_N^+Xe$  ( $N = 5–8$ ) complexes in the visible–near-ultraviolet range.<sup>86</sup> More recently, vibrational spectra of  $V_N^+Ar$  ( $N = 6–23$ ) have been reported in the 140–450- $\text{cm}^{-1}$  region,<sup>87</sup> which were analyzed to determine the geometrical structures of  $V_N^+$ .<sup>88</sup>

We discuss several outcomes of our studies of photodissociation dynamics by focusing in particular on electronic structures, chemical bonds, and magnetic properties of  $Ag_4^+$ ,  $Mn_N^+$ , and  $Cr_3^+$ , in the following subsection.

**II.3. Properties of Clusters Derived from Electronic Spectra and Dissociation Dynamics.** *II.3.1. Geometric and Electronic Structures.* We present photodissociation dynamics of a silver tetramer cation,  $Ag_4^+$ , to illustrate practical collaboration with theoretical studies to obtain geometric and electronic structures. A photodissociation action spectrum was measured by the experimental setup shown in Figure 1. Mass-selected  $Ag_4^+$  was irradiated with a tunable laser pulse from an optical parametric oscillator and photofragment ions were



**Figure 2.** Photodissociation action spectra of  $Ag_4^+$ : (a)–(c) partial cross sections for the processes producing  $Ag_3^+$ ,  $Ag_2^+$ , and  $Ag^+$ , respectively; (d) total cross section. The solid curves represent fitting to Gaussian profiles.

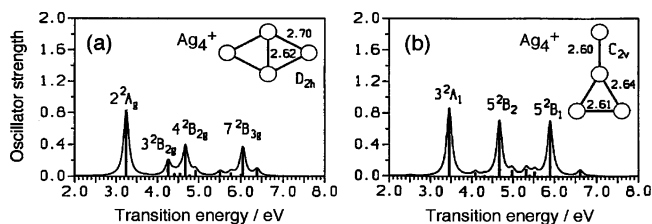


**Figure 3.** Absorption spectra of  $Ag_4^+$  simulated by ab initio calculations: (a) the most stable  $D_{2h}$  structure; (b) the second most stable  $C_{2v}$  structure. Reprinted with permission from ref 92. Copyright 1999, American Institute of Physics.

detected after mass analysis. A TOF profile of neutral photofragments was recorded as well for the analysis of KER.<sup>80</sup>

Partial photodissociation cross sections are shown in Figures 2a–c for each size of photofragment ions in the photon-energy range between 2 and 5 eV. These cross sections are added together to construct a spectrum of total cross sections shown in Figure 2d. Three major peaks are discernible at 3.13, 4.00, and 4.36 eV with line widths less than 0.1 eV. As the dissociation energy of  $Ag_4^+$  is estimated to be  $D(Ag_3^+ \dots Ag) = 1.27$  eV by a theoretical calculation,<sup>89</sup> clusters dissociate readily from these photoexcited states; the total photodissociation cross section is equivalent to photoabsorption cross section. Similar spectra have been reported for rare-gas and molecular complexes,  $Ag_4^+Kr_m$  and  $Ag_4^+(N_2)_m$ , in narrower spectral regions.<sup>90,91</sup> The similarity in the narrow line widths observed implies that the present  $Ag_4^+$  is as cold as the rare-gas complexes; the temperature is estimated to be below 150 K. Here the “temperature” of a cluster is defined as an internal

energy divided by internal degrees of freedom and the Boltzmann constant.

The photoabsorption spectrum, Figure 2d, is compared with the results of theoretical studies,<sup>89,92</sup> as described in detail in Supporting Information S2.1. Briefly, simulated absorption spectra are obtained for two isomers shown in Figure 3; a rhombic ( $D_{2h}$ ) structure in a  ${}^2B_{2u}$  electronic state, which is the most stable, and a T-shape ( $C_{2v}$ ) one in  ${}^2A_1$ , which is higher by 0.31 eV in total energy. Among the two spectra, the rhombic one, Figure 3a, reproduces the experimental spectrum well both in the transition energies and in the oscillator strengths; the absorption peaks at 3.13, 4.00, and 4.36 observed in our experiments are assigned to  $2^2A_g$ ,  $3^2B_{2g}$ , and  $4^2B_{2g}$ , respectively. These agreements confirm that  $Ag_4^+$  produced in the experiment has the most stable  $D_{2h}$  structure.

The spectra for different dissociation channels, Figures 2a–c, indicate that these dissociation processes occur in a non-statistical manner, as discussed in Supporting Information S2.2 on the basis of the dissociation energies obtained by the theoretical studies. Production of  $Ag_2^+$  proceeds via fission,  $Ag_4^+ \rightarrow Ag_2^+ + Ag_2$ , rather than via sequential evaporation,  $Ag_4^+ \rightarrow Ag_3^+ + Ag \rightarrow Ag_2^+ + 2Ag$ ;  $Ag^+$  is produced by the process  $Ag_4^+ \rightarrow Ag^+ + Ag_3$ . The dissociation processes of larger clusters,  $Ag_N^+$  ( $N = 8-21$ ), on the other hand, have been interpreted by a statistical model.<sup>19</sup> The present nonstatistical behavior is in contrast to most of other cases, where thermal mechanisms dominate the processes.

The dissociation dynamics is investigated by KER measurements. The velocity distributions of neutral fragments obtained from TOF profiles are shown in Figure 4, where the excitation photon energies are 3.11, 4.01, and 4.36 eV for Figures 4a–c, respectively. The data for two polarization conditions, either parallel or perpendicular with respect to the cluster-beam axis, are identical, indicating isotropic fragmentation. In these measurements, only one isotopomer,  $(^{107}Ag_2^{109}Ag_2)^+$ , was irradiated by focusing the excitation-laser beam with a cylindrical lens in the direction of the ion beam to obtain sufficient resolution in the TOF data. All the profiles are significantly broader than the initial-velocity distribution of the parent cluster ion shown by a dashed line in Figure 4c; the broadening is predominantly due to KER. The distributions were well reproduced by two Gaussian profiles for 3.11- and 4.01-eV excitation, but only a single Gaussian component explained the data for 4.36-eV excitation. The single and bimodal behaviors in production of  $Ag_2$  (in the latter) and  $Ag$  (in the former), respectively, are consistent with the  $D_{2h}$  structure of  $Ag_4^+$  as discussed in Supporting Information S2.3; the study of dynamics provides support for determination of the geometrical structure.

The velocity profiles are further converted to distributions of translational kinetic energies carried by both neutral and ionic fragments, as shown in Figures 4a'–c'. The fragmentation at 3.11 (4.01)-eV excitation is associated with fast and slow components with average translational kinetic energies of 0.29 (0.51) and 0.06 (0.06) eV, respectively. The average of the total translational energy is 0.40 eV at 4.36-eV excitation. From these kinetic energies of photofragments and bond dissociation energies,<sup>89</sup> the average of the total internal energies deposited in the fragments are estimated as shown in Table 1. It was found that more than 80% of the excess energy goes to internal energy of fragments. The cluster fragments must be highly excited in vibration, because the excess energy is not high enough for electronic excitation of silver atom, dimer, and trimer (more than 3 eV is necessary).

In summary, the present study rationalizes the collaboration between optical experiments and the state-of-the-art theoretical

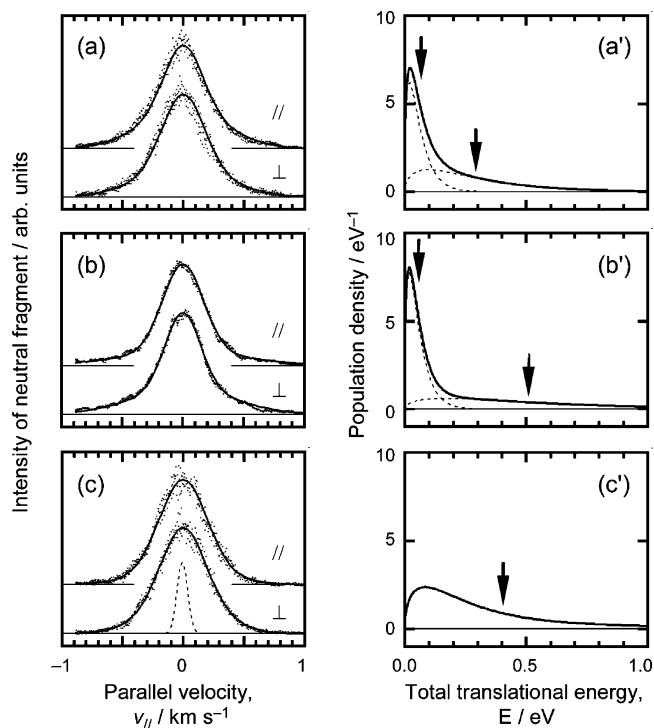


**Figure 4.** (a)–(c) Intensities of neutral photofragments produced upon photodissociation of  $Ag_4^+$  as a function of the velocity component parallel to the cluster-ion beam axis in the center-of-mass frame. Photon energies are (a) 3.11, (b) 4.01, and (c) 4.36 eV. The polarization plane of the laser beam was either parallel (||) or perpendicular ( $\perp$ ) to the cluster-beam axis. Dots are experimental data. Solid curves represent fitting of each profile to a summation of two Gaussian functions. A dashed line in (c) shows a velocity distribution of the parent cluster ion. (a')–(c') Distributions of translational kinetic energies carried by both anionic and neutral fragments derived from (a)–(c), respectively. The fragmentation channel is assumed as (a', b')  $Ag_4^+ \rightarrow Ag_3^+ + Ag$  and (c')  $Ag_4^+ \rightarrow Ag_2^+ + Ag_2$ . Dashed lines in (a') and (b') show contributions of two components. Arrows indicate average energies for each component.

**TABLE 1: Energy Redistribution in  $Ag_4^+$  Following Photoexcitation to Three Excited Electronic States<sup>a</sup>**

	peak 1		peak 2		peak 3
photon energy/eV	3.11		4.01		4.36
dominant fragments	$Ag_3^+, Ag$		$Ag_3^+, Ag$		$Ag_2^+, Ag_2$
$E_{diss}/eV$	1.27		1.27		2.56
$E_{excess}/eV$	1.84		2.74		1.80
$\langle E_{trans} \rangle / eV$	slow	fast	slow	fast	0.40
	0.06	0.29	0.06	0.51	
	(3%)	(16%)	(2%)	(19%)	(22%)
$\langle E_{int} \rangle / eV$	1.78	1.55	2.63	2.23	1.40
	(97%)	(84%)	(98%)	(81%)	

<sup>a</sup>  $E_{diss}$ : binding energy between the dominant fragments obtained by theoretical studies.<sup>89</sup>  $E_{excess}$ : excess energy obtained by subtracting  $E_{diss}$  from the photon energy.  $\langle E_{trans} \rangle$ : average of the total translational energy carried by both the neutral and the ionic fragments, which is indicated by arrows in Figures 4a'–c'. The left and right columns give the slow and fast components, respectively, for bimodal KER.  $\langle E_{int} \rangle$ : internal energy deposited to the fragments as obtained by  $E_{excess} - \langle E_{trans} \rangle$ . The parentheses show branching ratios of energies with respect to  $E_{excess}$ .

studies, where the most stable species found by theory provides quantitative agreements with experiment. The fact that the electronic structure is described by the molecular-orbital theory implies that the excitation is due to transition of a single electron between molecular orbitals rather than collective excitation of electrons illustrated by surface-plasmon resonance on the basis of the jellium model,<sup>4,5</sup> where valence electrons are assumed

to be confined in a potential well formed by ionic cores of constituent atoms. The jellium-like behavior has been found for  $\text{Ag}_N^+$  generated by a sputtering-cluster-ion source, where a broad spectral width greater than 0.5 eV was observed.<sup>93–95</sup> It is estimated that these cluster ions possess high internal energy (more than 400 K in temperature). On the other hand, the temperature of the present  $\text{Ag}_4^+$  generated by laser vaporization is estimated below 150 K; the jellium behavior may not appear at low temperatures due to suppression of thermally activated motions. A similar molecular behavior has been found for  $\text{Ag}_N$  embedded in matrices,  $\text{Ag}_8$  in a liquid He droplet at 0.37 K probed by R2PI,<sup>96</sup> and  $\text{Ag}_{3,4,8,9}$  in an Ar matrix at 25 K observed by fluorescence;<sup>20–23</sup> these spectra are well explained by the molecular-orbital theory.<sup>97</sup> As discussed for free sodium cluster ions,  $\text{Na}_N^+$ ,<sup>98,99</sup> not only the size but also the temperature (internal energy) is an important parameter for the behavior of electrons in metal clusters.

**II.3.2. Bond Dissociation Energies.** A bond dissociation energy can be determined from a threshold energy of dissociation, where CID is used most frequently.<sup>24</sup> Alternatively used is photodissociation, which has an advantage in that the deposited energy is well-defined by the photon energy instead of collisional energy transfer. However, the following should be noted: First, the threshold should lie in an absorption band of the cluster; the dissociation energy is just bracketed otherwise.<sup>40</sup> Second, the threshold is not sharp but broadened and deviated from the bond dissociation energy because of (1) a distribution of internal energies of initial clusters and (2) a finite lifetime of excited clusters depending on an excess energy.<sup>100</sup> For clusters larger than about  $N = 10$ , the latter effect is so large that the lifetime of the photoexcited state may be measured instead.<sup>16–18</sup> We discuss here the determination of bond dissociation energies of manganese cluster ions.<sup>101,102</sup>

Manganese cluster ions are one of the suited targets for determination of their bond dissociation energies by the photodissociation technique, because it is so weakly bound that one or two atoms are released sequentially even in the visible range; they show broad absorption bands as well. Results of  $\text{Mn}_3^+$  are shown in Figure 5. Partial dissociation cross sections were measured as the photon energy was varied from 1.2 to 2.8 eV, as shown in Figure 5a. As is manifested in the branching fraction to the  $\text{Mn}^+$  channel shown in Figure 5b,  $\text{Mn}_2^+$  is produced dominantly below 2.0 eV, whereas  $\text{Mn}^+$  gradually takes over above it. This monotonic change in the branching fraction implies that the dissociation of  $\text{Mn}_3^+$  proceeds via sequential loss of Mn atoms in accordance with the excess energy.

The onset behavior of the  $\text{Mn}^+$  formation in the region 1.9 – 2.2 eV is analyzed on the basis of a model that internally hot clusters dissociate with excess energy less than the dissociation threshold. The branching fraction,  $R(E_p)$ , is fitted to a formula,  $R(E_p) = \exp[(E_p - E_{\text{th}})/\langle E_{\text{int}} \rangle]$  (at  $E_p < E_{\text{th}}$ ), by assuming the Boltzmann distribution for the population in internally hot levels, where  $E_p$  is the photon energy,  $E_{\text{th}}$  is the threshold energy for two-atom release, and  $\langle E_{\text{int}} \rangle$  is the average internal energy of  $\text{Mn}_3^+$  as produced. This model well explains the onset behavior of the branching fraction, as shown by the thick solid curve in Figure 5b. The threshold energy,  $E_{\text{th}}$ , is determined to be  $2.22 \pm 0.05$  eV. Because the excess energy needed for a trimer to dissociate in the present experimental time scale of about 20  $\mu\text{s}$  is negligibly small, as shown in Supporting Information S1, the threshold energy corresponds to the binding energy per atom,  $E_b(\text{Mn}_3^+)$ . Thus  $E_b(\text{Mn}_3^+) = 2.22 \pm 0.05$  eV. The bond dissociation energy of  $\text{Mn}_3^+$ ,  $D_0(\text{Mn}_2^+ \dots \text{Mn})$ , is further derived to be  $0.83 \pm 0.05$  eV, as the bond dissociation energy of the dimer ion,  $D_0(\text{Mn}^+ \dots \text{Mn})$ , is

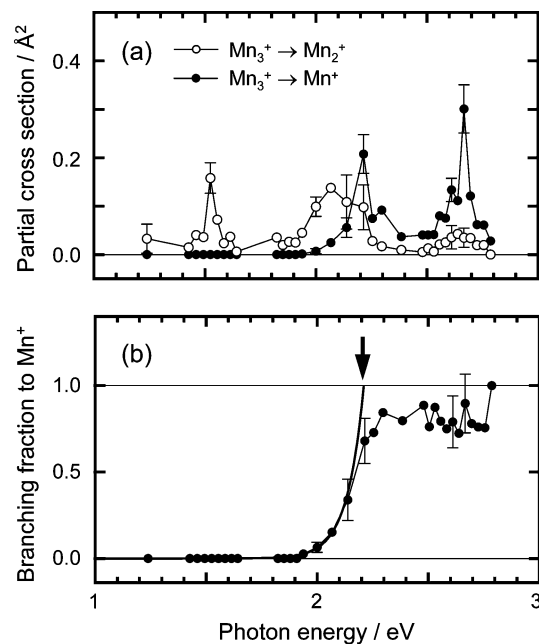


**Figure 5.** (a) Spectra of the partial photodissociation cross sections of  $\text{Mn}_3^+$ : open (solid) circles are for the dissociation channel to  $\text{Mn}_2^+$  ( $\text{Mn}^+$ ). (b) Branching fraction of the  $\text{Mn}^+$  channel as a function of the photon energy. The thick solid curve fits the onset behavior, which is explained by the internal-energy distribution of primary  $\text{Mn}_3^+$ . The arrow indicates the threshold energy of the  $\text{Mn}^+$  formation from  $\text{Mn}_3^+$ .

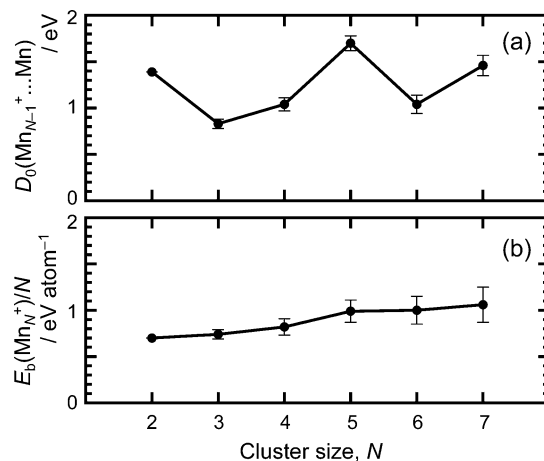


**Figure 6.** (a) Bond dissociation energy,  $D_0(\text{Mn}_{N-1}^+ \dots \text{Mn})$ , and (b) binding energy per atom,  $E_b(\text{Mn}_N^+)/N$ , of  $\text{Mn}_N^+$  plotted as a function of the cluster size  $N$ .  $E_b(\text{Mn}_N^+)/N$  should be compared with the cohesive energy, 2.92 eV/atom, of bulk manganese.

reported to be 1.39 eV.<sup>103,104</sup> The fitting deduces the average internal energy;  $\langle E_{\text{int}} \rangle = 0.06 \pm 0.01$  eV, which corresponds to a temperature of 210 K.

Similar measurements were performed for other sizes,  $N = 4 - 7$ . All the cluster ions showed sequential evaporation up to two atoms in the photon-energy range below 2.8 eV. The threshold energies for two-atom loss were determined from the onset behavior, which was well fitted by a common temperature of about 200 K for all the sizes. The two-atom dissociation energies,  $D_0(\text{Mn}_{N-2}^+ \dots 2\text{Mn})$ , were obtained after compensation for the finite lifetime effect. Bond dissociation energies,  $D_0(\text{Mn}_{N-1}^+ \dots \text{Mn})$ , and binding energy per atom,  $E_b(\text{Mn}_N^+)$ , thus derived are plotted in Figure 6. These results show that the Mn–Mn bond is extremely weak compared with ordinary metal–metal bonds of other transition-metal elements, which usually ranges between 2 and 3 eV.<sup>105</sup> In particular, the binding energies per atom ranging from 0.7 to 1.1 eV/atom are far below the

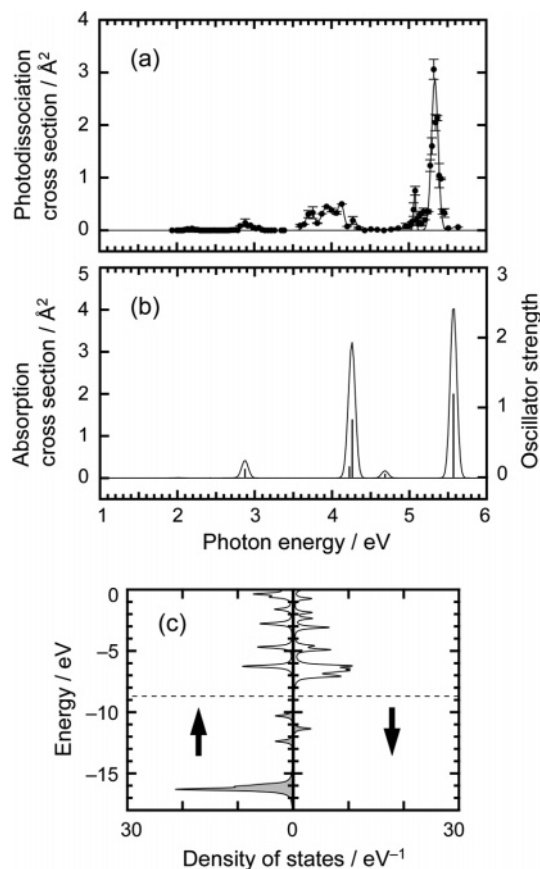


**Figure 7.** (a) Photodissociation action spectrum of  $\text{Mn}_2^+$ . Solid circles show data points. Error bars indicate statistical errors. The solid curve is a guide for the eye. (b) Simulated absorption spectrum of ferromagnetic  $\text{Mn}_2^+$  ( $2S + 1 = 12$ ). Bars indicate oscillator strengths of each transition. The solid curve is obtained by adding up all the transitions convoluted with a Gaussian profile of 0.1 eV FWHM. (c) Calculated density-of-states profiles for the majority and minority spins. Each level is convoluted with a Lorentzian profile of 0.2 eV FWHM. The dashed line indicates the chemical potential, below which the orbitals are occupied.

bulk cohesive energy, 2.92 eV/atom. The  $\text{Mn}_N^+$  in this size range are characterized by weak metal–metal bonds primarily due to 4s electrons; 3d electrons are localized on each atomic site and give rise to a large local spin. The weak chemical bond in  $\text{Mn}_N^+$  is correlated with the magnetic properties discussed below.

**II.3.3. Magnetic Properties.** The electronic structures obtained by the interplay between spectroscopic experiments and theoretical analyses provide their materials properties. From the point of a view of novel magnetism, we focus on manganese cluster ions.<sup>106,107</sup>

The photodissociation action spectrum of  $\text{Mn}_2^+$  is shown in Figure 7a in the photon-energy range between 1.9 and 5.6 eV. As the bond dissociation energy is estimated to be 1.39 eV, prompt dissociation of  $\text{Mn}_2^+$  is ensured. The spectrum is thus equivalent to an optical absorption spectrum, which is characterized by major optical transitions observed at 5.3, 5.1, around 4.0, and 2.9 eV. The spectrum was analyzed by ab initio calculations as described in Supporting Information S3. Figure 7b shows the result of the calculation; the bars indicate transition energies and oscillator strengths, whereas the solid curve is obtained from the transition lines convoluted with a Gaussian profile with full width at half-maximum (FWHM) of 0.1 eV, as observed by the experiment. The simulation is in reasonable agreement with the experimental spectrum both in the transition energies and in the cross sections, except for the broadened

absorption peak around 4.0 eV in the experiment; the excited electronic states of the major transitions are assigned to  $^{12}\Sigma_u^+$  (2.87),  $^{12}\Pi_u$  (4.22),  $^{12}\Sigma_u^+$  (4.26), and  $^{12}\Pi_u$  (5.57 eV).

From the present calculations rationalized by the agreement with the experimental result, the ground electronic state of  $\text{Mn}_2^+$  is found to be  $^{12}\Sigma_g^+$  with a bond length of 3.01 Å and a binding energy of 1.68 eV. The bond length is much longer than the nearest neighbor distance in bulk manganese (2.24 Å),<sup>108</sup> whereas it is shorter than the bond length of the neutral dimer (3.4 Å) in rare-gas matrices.<sup>109</sup> The large spin multiplicity suggests a ferromagnetic Mn–Mn spin coupling. The electronic structure is shown in Figure 7c. The peak in the majority spin located at about  $-16$  eV originates from ten 3d electrons. Three peaks located between  $-10$  and  $-13$  eV are of 4s electrons; two are in the majority and one is in the minority spin state. This electronic structure indicates that the chemical bond between the manganese atoms are formed by 4s electrons, whereas 3d electrons are localized on each atomic site and show local spin magnetic moments as large as  $5 \mu_B$  (Bohr magneton), which are coupled in a ferromagnetic manner through a 4s hole via strong s–d exchange interaction similar to the double-exchange scheme in the solid-state physics.<sup>110</sup> This picture provides intuitive explanation for the weak Mn–Mn bond and the ferromagnetic coupling of the local spins. The  $^{12}\Sigma$  ground state has also been found for  $\text{Mn}_2^+$  in a rare-gas matrix by ESR measurement.<sup>111</sup> The ESR experiment further showed that neutral  $\text{Mn}_2$  is antiferromagnetic,<sup>112</sup> suggesting the importance of the 4s hole in the present ferromagnetic interaction.

The photodissociation action spectrum of  $\text{Mn}_3^+$  was measured and analyzed in a similar manner. The experimental and simulated spectra are shown in Figures 8a,b, respectively. The simulation based on the most stable ground electronic state,  $^{17}\text{B}_2$ , reproduces the experimental spectrum well: intense peak at 3.2 eV in the experiment is assigned to the  $9^{17}\text{A}_1$  (3.37 eV) excited state; the peaks at 3.7 and 3.9 eV are to  $10^{17}\text{A}_1$  (3.57 eV) and  $12^{17}\text{A}_1$  (4.08 eV), respectively; and the broad peak at 2.2 eV is to  $4^{17}\text{A}_1$  (2.16 eV) and  $5^{17}\text{A}_1$  (2.39 eV). It should be noted that the peaks at 1.5 and 2.7 eV observed in the experiment (marked by asterisks in Figure 8a) are missing in the simulation; these peaks originate from a metastable isomer as suggested by temperature-dependence measurements, which do not appear in the present ground-state calculation.

It was thus found that  $\text{Mn}_3^+$  has spin multiplicity of 17,  $C_{2v}$  symmetry with an isosceles triangular structure and an apex bond angle of  $144^\circ$ , and the bond length of 3.03 Å. The binding energy was calculated to be 0.86 eV/atom, which is in reasonable agreement with the experimental result, 0.74 eV/atom, obtained in section II.3.2. The localized spin magnetic moments are  $5.2 \mu_B$  at the top-apex site and  $5.4 \mu_B$  at the two base sites, and all the spins couple ferromagnetically to give rise to a total spin magnetic moment of  $16 \mu_B$ . The electronic structure, Figure 8c, illustrates fifteen 3d electrons occupying the majority spin state located at about  $-15$  eV and three and two 4s electrons in majority- and minority-spin state, respectively. The positive charge due to one missing 4s electron is delocalized to form weak covalent bonds in a manner similar to  $\text{Mn}_2^+$ .

The analyses of larger clusters,  $\text{Mn}_N^+$  ( $N \geq 4$ ), are difficult in the present stage, because their spectra show a very broad feature without any characteristic structures probably due to coexistence of structural isomers; that makes comparison between experiment and theory not decisive. The computational study of  $\text{Mn}_4^+$  resulted in nearly degenerate isomers ( $C_{3v}$  symmetry with spin magnetic moments of 9 and  $21 \mu_B$ ) showing

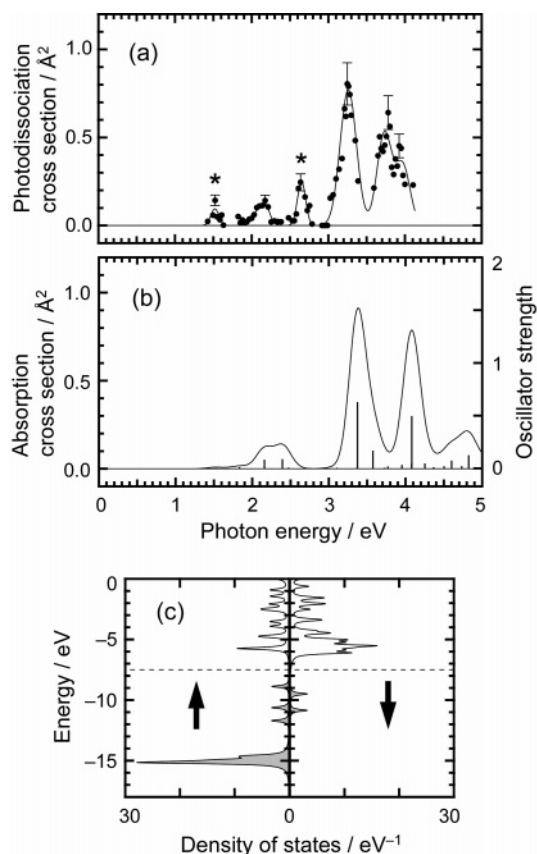


**Figure 8.** (a) Photodissociation action spectrum of  $\text{Mn}_3^+$ . Asterisks denote contributions from metastable isomers, which are weaker at lower temperatures of the cluster-growth room. (b) Simulated absorption spectrum of ferromagnetic  $\text{Mn}_3^+$  ( $2S + 1 = 17$ ). The solid curve is obtained by convolution with a Gaussian profile of 0.25 eV FWHM. (c) Calculated density-of-states profiles for the majority and minority spins. (See Figure 7 for the detailed caption.)

very different spectra, neither of which explains the experimental spectrum alone.<sup>113</sup> Low-temperature experiments are required in the future.

The ferromagnetic spin coupling found for  $\text{Mn}_2^+$  and  $\text{Mn}_3^+$  is in striking contrast to the antiferromagnetic bulk manganese. As the ferromagnetic spin coupling is primarily due to the weak Mn–Mn bond, it is reasonable that the spin coupling turns to antiferromagnetic as the size increases. More significant contribution of the 3d electrons to the covalent bond at larger sizes explains the tendency of larger binding energies, shorter bond lengths, smaller local spins, and more favorable antiferromagnetic spin coupling. Studies of magnetic properties of free manganese clusters,  $\text{Mn}_N$ , have been performed by the Stern–Gerlach type experiment, where the deflection of a  $\text{Mn}_N$  beam in an inhomogeneous magnetic field is measured to obtain a total magnetic moment of the cluster.<sup>114,115</sup> It was found that  $\text{Mn}_N$  ( $N = 5 - 99$ ) exhibit a ferrimagnetic order; i.e., the spins couple in an antiparallel manner but do not cancel out. These findings by spectroscopy and beam-deflection experiments have been stimulating many theoretical studies to clarify the magnetism of manganese clusters in the small size range, in particular, to elucidate the transition from ferro- to ferrimagnetism by size, which is still an open question.<sup>116–125</sup>

**II.3.4. Magnetic Interaction vs Geometrical Structure.** In connection with the novel magnetism revealed for the manganese cluster ions, we have recently found that magnetic interaction in turn influences the structure of a cluster of chromium.<sup>126</sup> Because of the electronic configuration,  $3d^5 4s^1$ ,

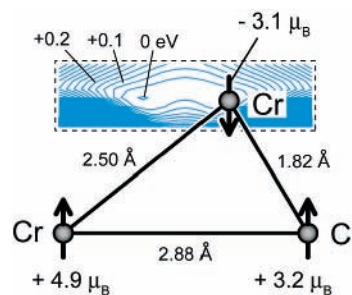


**Figure 9.** Optimized geometrical structure of  $\text{Cr}_3^+$  obtained by the DFT (density-functional theory) calculation. The bond lengths and the Mulliken atomic spin densities on each atom are indicated. The contour map shows the potential-energy surface at a 0.04 eV interval for the top apex atom; the base atoms stay at the same positions as the top atom moves.

of the Cr atom, the dimer,  $\text{Cr}_2$ , forms a singlet ground state with local spins on the Cr sites coupled in an antiferromagnetic manner. Therefore, addition of the third atom (or ion) to the dimer introduces spin frustration, where two atoms out of the three have spin up and the other down. As it is known that the metastable dimer in a ferromagnetic (up–up) configuration favors a bond length longer than that of the ground state (up–down), it is anticipated that the spin-down atom experiences a double-well-type potential-energy surface with two potential minima satisfying an equilibrium up–down bond length with either of the two spin-up atoms. If the potential barrier is low enough, the structure may be floppy and fluctuating at finite temperatures. The trimer ion,  $\text{Cr}_3^+$ , was investigated by photodissociation experiment and ab initio calculations.<sup>126</sup>

Figure 9 shows the optimized geometrical structure of  $\text{Cr}_3^+$  with spin multiplicity of six ( $2S + 1 = 6$ ). The structure has a  $C_s$  symmetry with the spin-down atom located closer to one of the spin-up atoms, where the short bond length is almost the same as that of the dimer. The contour map shows the change in total energy as a function of the location of the spin-down atom, whereas the spin-up base atoms stay at the same positions. It is symmetrical with respect to the perpendicular bisector of the base atoms. The barrier height for the spin-down atom to be relocated from the right minimum to the left one was calculated to be only about 0.02 eV, which is lower than the zero-point energy, 0.03 eV, of vibration. This result implies that  $\text{Cr}_3^+$  has an intrinsically floppy structure due to the spin frustration. This feature was evidenced by experiment as well; the photodissociation spectrum in the range from 1.3 to 5.5 eV could not be explained by the spectrum simulated for the  $C_s$  structure alone, but a reasonable agreement was obtained by considering a mixture of two isomer spectra, i.e., the most-stable  $C_s$  structure and a metastable one with a  $C_{2v}$  symmetry, which is only 0.01 eV higher in total energy.

### III. Surface-Impact Excitation

**III.1. Dynamics Following Collisional Excitation.** In contrast to electronic excitation by a photon, collisional excitation induces collective motions of constituent atoms of a cluster as well. For example, MD simulations identify breathing, quadrupole spheroidal, and quadrupole torsional vibrations of argon clusters as fundamental modes of collective vibration.<sup>25,26</sup> Excitation of such collective motions has indeed been evidenced experimentally, e.g., by He atom collision of  $\text{Ar}_N^{27,28}$  and  $\text{Na}_N^+$ <sup>29,30</sup> as described in detail in Supporting Information S4. In contrast to single collision with an atom, impact on a solid surface induces even more extraordinary reaction dynamics, where impulsive multiple collision causes a concerted motion

of constituent atoms leading to superheating, site-specific bond splitting, a shock wave, etc.

The experiment of cluster collision with a solid surface was first performed in the 1970s on large clusters of  $\text{He}_N$ ,  $(\text{H}_2)_N$ , and  $(\text{N}_2)_N$  with  $N = 10^4$ – $10^5$  produced by supersonic expansion.<sup>127</sup> Secondary clusters recoiling from a stainless-steel surface at various temperatures and incidence angles were analyzed for average sizes, velocities, and angular distributions. This pioneering work was followed by more quantitative studies on similar van-der-Waals clusters.<sup>128–130</sup> These low-energy collision experiments (10–100 meV per atom or molecule) revealed the following three processes: (1) Constituent atoms/molecules faced to a surface are trapped once on the surface and evaporate into a surface-normal direction after thermalization. (2) The internal energy upon collision is transferred from the surface contact region to the remaining part of the cluster and promotes evaporation of atoms/molecules from the outer region into near specular angles. (3) After the second evaporation process, the remaining part of the cluster is cold enough to survive as a cluster, which recoils into a tangential direction from the surface (supraspecular reflection) just like the Leidenfrost phenomenon<sup>131,132</sup> (a jumping liquid droplet on a hot plate).

New chemistry arises at elevated collision energies. A MD simulation was performed for  $\text{Ar}_{561}$  impinging on a NaCl surface at a translational kinetic energy of 2 eV/atom (3 km/s; a hyperthermal condition), which showed that the cluster reaches a local temperature as high as 4000 K, a pressure of 10 GPa, and a density of atoms 1.5 times higher than that of normal liquid Ar; these phenomena occur transiently at an instant of collision.<sup>133</sup> The translational energy is dissipated even as a shock wave upon more energetic collisions;<sup>134,135</sup> the cluster cannot survive any more above a threshold impact energy (about 10 km/s in velocity) and fragments into a number of monomers (shattering) within 100 fs after collision. Levine and co-workers have pointed out that shattering is a new type of phase transition driven by entropy of the system, as predicted by theory<sup>136</sup> and evidenced by experiments.<sup>137–139</sup> An important phenomenon from chemical points of view is the four-center reaction initiated for reactant molecules solvated by rare-gas atoms;  $\text{H}_2 + \text{I}_2$  reaction and unimolecular isomerization from norbornadiene to quadricyclane have been reported<sup>140</sup> as well as NO formation from  $\text{N}_2$  and  $\text{O}_2$ <sup>33</sup> mentioned in Introduction. In these reaction processes, solvent Ne atoms play roles in three ways: (1) Impose a geometrical constraint to the reactant molecules before impact so that they are arranged favorably for the reaction. (2) Transfer the impact energy efficiently to the reactants through multiple collisions during impact. (3) Stabilize the reaction products by carrying away the excess thermal energy after impact. These theoretical studies exemplify the importance of cluster-impact chemistry as a new class of reaction processes.

One might think that the cluster-impact chemistry would be related to the molecular-beam study of surface chemistry,<sup>141</sup> where the importance of translational energy was demonstrated in chemisorption of an impinging molecule and in that of a physisorbed molecule assisted by inert-gas collision. However, multiple collision is essentially important in the cluster-impact process for initiating a concerted motion, whereas the latter is concerned with single-collision processes.

The specificities of the cluster-impact processes predicted above are (1) impulsive nature of the impact at hyperthermal velocities and (2) excitation of a specific reaction mode, which lead to chemical environments with extremely high temperature and pressure enabling extraordinary bond formation and breaking. We have developed experimental techniques to observe

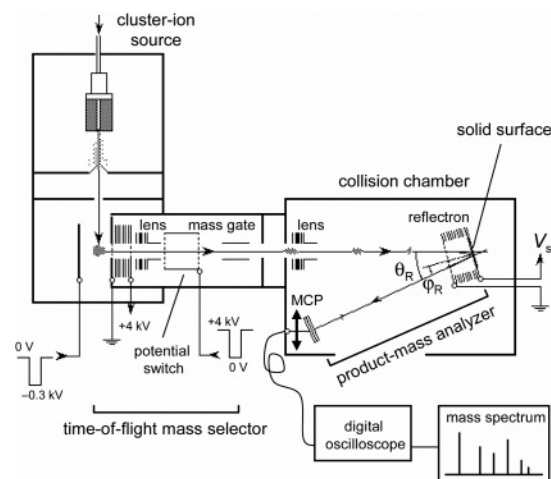


**Figure 10.** Experimental setup for size-selected cluster-ion impact on a solid surface equipped with a tandem TOF mass spectrometer.

these chemical processes and obtained the following major findings described in this section: (1) pickup reaction of aluminum cluster anions,  $\text{Al}_N^-$ , on a graphite surface under a super-high local temperature; (2) contrasted fragmentation processes of  $\text{Al}_N^-$  and  $\text{Si}_N^-$  ascribable to the nature of the chemical bonds; (3) a site-specific bond splitting in solvated cluster anions,  $\text{I}_2^-(\text{CO}_2)_N$ .

**III.2. Experimental Procedures.** Figure 10 shows our experimental setup equipped with a tandem TOF mass spectrometer.<sup>142–144</sup> Briefly, cluster anions are generated in a pulse either by the laser-vaporization technique for  $\text{Al}_N^-$  and  $\text{Si}_N^-$  or by secondary electron attachment by electron impact on a supersonic jet of  $\text{CO}_2$  containing  $\text{I}_2$  vapor seeded by a He gas for  $\text{I}_2^-(\text{CO}_2)_N$ . The cluster anions thus produced are extracted by a pulsed electric field, size-selected by a primary TOF mass spectrometer, and admitted into a reflectron with a solid surface mounted on its back. The incoming cluster anion is decelerated by an electric field inside the reflectron and impinges on the surface. The impact energy,  $E_c$ , is varied by adjusting a bias voltage,  $V_s$ , applied to the surface. Product anions scattered off the surface are accelerated by the same electric field and mass-analyzed by a secondary TOF spectrometer. The angle between the first (incoming) and the second (outgoing) flight path,  $\theta_R$ , is varied between near  $0^\circ$  and  $8^\circ$  by translating the ion detector. The angle between the surface normal and the second flight path,  $\phi_R$ , is varied between  $0^\circ$  and  $4^\circ$  by rotating the reflectron. At  $\phi_R = 0^\circ$ , product anions scattered into the surface normal are detected, and at  $\phi_R = \theta_R/2$ , anions reflected elastically into the specular direction are detected. The angular distribution of the product anions are thus measured. One should note that  $\phi_R$  is not an actual angle of reflection because the anions are forced to travel along a parabolic trajectory inside the reflectron. The actual angle of reflection is given by  $\tan^{-1}(v_{\parallel}/v_{\perp})$ , where  $v_{\parallel}$  and  $v_{\perp}$  are the surface-tangent and the surface-normal recoil velocities, respectively. The experiments focused on anions because cations had low scattering yields due to high probability of neutralization via electron transfer from the solid surface.

**III.3. Surface Impact of Metal and Semiconductor Clusters.**  
**III.3.1. Impact-Induced Reaction of Aluminum Cluster Anions: Pickup of Surface Atoms.** A chemical reaction under a high temperature created by cluster impact was observed for aluminum cluster anions on a graphite surface.<sup>145,146</sup> Figure 11a shows TOF mass spectra of anions produced from  $\text{Al}_{13}^-$ . The position of the ion detector and the angle of the reflectron were adjusted so that all the product anions were detected simulta-

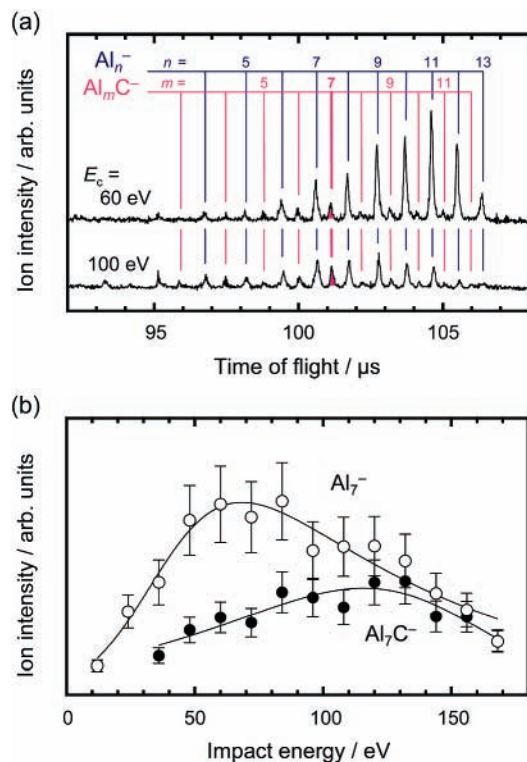


**Figure 11.** (a) TOF mass spectra of product anions,  $\text{Al}_n^-$  and  $\text{Al}_m\text{C}^-$ , produced by impact of  $\text{Al}_{13}^-$  on a graphite surface. The impact energies are 60 and 100 eV. (b) Intensities of product anions,  $\text{Al}_7^-$  (open circles) and  $\text{Al}_7\text{C}^-$  (closed circles), as a function of the impact energy of  $\text{Al}_{13}^-$ . The solid curves are guides for the eye.

neously ( $\theta_R = 2.6^\circ$  and  $\varphi_R = 0^\circ$ ). Not only fragment anions,  $\text{Al}_n^-$ , but also binary cluster anions,  $\text{Al}_m\text{C}^-$ , are produced as a result of pickup reactions. The peak of  $\text{Al}_7\text{C}^-$  is the most intense among those with different  $m$ 's, indicating that  $\text{Al}_7\text{C}^-$  is a stable product anion. The selective formation of  $\text{Al}_7\text{C}^-$  was a common behavior observed also for other sizes of  $\text{Al}_N^-$  ( $8 \leq N \leq 12$ ). Similar abundance of  $\text{Al}_7\text{C}^-$  has been observed in a mass spectrum of  $\text{Al}_N\text{C}^-$  produced by laser vaporization of an aluminum rod coated with carbon<sup>147</sup> or in the presence of methane,<sup>148</sup> and its stability has been confirmed by a reaction experiment against oxygen<sup>148</sup> and ab initio calculations.<sup>149,150</sup> These related studies suggest that the local temperature created upon present cluster impact is comparable to that prepared by laser vaporization. The high-temperature environment is a necessary condition for annealing of reaction products to produce the most stable species abundantly.

The ion intensities of  $\text{Al}_7^-$  and  $\text{Al}_7\text{C}^-$  are plotted in Figure 11b as a function of the collision energy. The yield of  $\text{Al}_7^-$  reaches its maximum at  $E_c = 70$  eV, whereas that of  $\text{Al}_7\text{C}^-$  does at 120 eV. The additional energy, 50 eV, needed for the production of  $\text{Al}_7\text{C}^-$  is reasonable for liberating carbon atoms for the pickup reaction; as many as four carbon atoms can be liberated because the dissociation energy of the C–C bond in graphite is about 5 eV. The additional energy is correlated as well with the threshold energy in the range of 40–80 eV for creating a defect in a graphite by rare-gas ion sputtering.<sup>151</sup>

It should be noted that similar impact of silicon cluster anions,  $\text{Si}_N^-$ , did not show any reaction with surface atoms. Cationic ones,  $\text{Si}_N^+$ , have been reported to be nonreactive as well.<sup>152</sup> These findings motivate the experiments described in the next subsection, where the local temperature created upon impact and the redistribution processes of the translational energy are

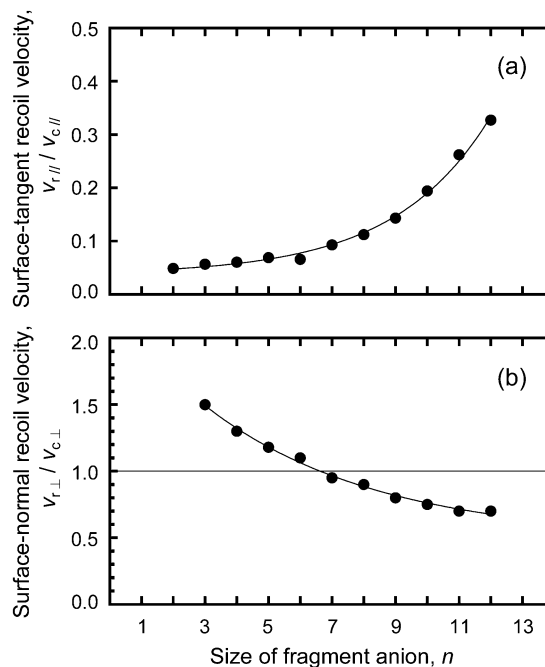


**Figure 12.** (a) Surface-tangent and (b) surface-normal components of recoil velocities (normalized by those of impact velocities) of fragment anions,  $\text{Al}_n^-$ , produced from  $\text{Al}_{13}^-$  upon impact on a silicon surface at 80 eV. The solid curves are guides for the eye.

measured and analyzed for  $\text{Al}_N^-$  and  $\text{Si}_N^-$  to illustrate their distinct features.

**III.3.2. Energy Redistribution Processes: Aluminum vs Silicon Cluster Anions.** III.3.2.a. Impact of Aluminum Cluster Anions. Detailed investigation of the impact process was performed for  $\text{Al}_{13}^-$  impinging on a silicon surface instead of graphite; the silicon had an advantage of relatively straightforward analysis of the data, because only dissociation products were observed without any pick-up reaction.<sup>143</sup> By the experimental procedures described in Supporting Information S5, recoil velocities of fragment anions with size  $n$  are obtained as shown in Figure 12; the surface-tangent,  $v_{t||}(n)$ , and the surface-normal,  $v_{t\perp}(n)$ , components are normalized by the corresponding incidence impact velocities,  $v_{c||}$  and  $v_{c\perp}$ , of  $\text{Al}_{13}^-$ , respectively. The velocity of the fragment anion depends strongly on its size. This fact implies that the dissociation proceeds during interaction of the parent cluster anion with the surface rather than in a unimolecular manner after scattering.

On the basis of this picture, these results are interpreted as follows: The tangential component of the recoil velocity is considerably smaller than the incident velocity. This behavior indicates that there is a momentum-loss mechanism effective particularly in the tangential direction; a drag force is exerted during the interaction with the surface. In this simple model, a fragment anion with a slower tangential velocity is considered to spend longer time on the surface before recoil. Because the drag force is proportional to the velocity in energy-dissipation processes,<sup>153</sup> the tangential velocity decreases exponentially as the time elapses. Therefore, the residence time,  $\tau_{\text{res}}(n)$ , of a cluster on the surface for producing a fragment anion of size  $n$  is related to the incidence and recoil tangential velocities as  $\tau_{\text{res}}(n) \propto -\ln(v_{t||}(n)/v_{c||})$ ; a smaller fragment anion leaves the surface after a longer residence time. On the other hand, the normal recoil velocity has an opposite tendency; a smaller fragment anion has a higher velocity. This implies that the fragment anion leaves the surface with thermal energy determined by a local temperature created upon impact, which is estimated to

**TABLE 2: Energy Redistribution in  $Al_N^-$  and  $Si_N^-$  Following Impact on a Silicon Surface<sup>a</sup>**

	$Al_N^-$	$Si_N^-$
major dissociation process	evaporation	fission
residence time on surface	long	short
energy redistribution		
$E_{trans}^{frag}/E_c$	20–10%	~40%
$E_{int}^{cluster} (=E_{diss} + E_{trans}^{evap} + E_{int}^{frag})/E_c$	20–45%	~20%
$E_{int}^{surface}/E_c$	60–45%	~40%
chemical bond in solid	metallic	covalent
mechanical property of solid	ductile, malleable	brittle

<sup>a</sup>  $E_{trans}^{frag}$ : translational energy of fragment cluster(s).  $E_{diss}$ : dissociation energy.  $E_{trans}^{evap}$ : total translational energy of evaporated atoms.  $E_{int}^{frag}$ : internal energy of fragment cluster(s).  $E_{int}^{surface}$ : internal energy of surface.  $E_c$ : impact translational energy ( $=E_{trans}^{frag} + E_{int}^{cluster} + E_{int}^{surface}$ ).

be  $(1.0 \pm 0.2) \times 10^4$  K at the impact energy of 80 eV.<sup>143</sup> Creation of a super-high local temperature is thus evidenced.

The scenario of the fragmentation process of  $Al_N^-$  is summarized as follows: Most of the translational energy is converted to thermal energy at the moment of impact, which creates a local temperature as high as  $10^4$  K. The incident cluster glides along the surface, is decelerated by a drag force, where constituent atoms evaporate sequentially during the process; and a fragment anion leaves the surface at a thermal velocity. Small fragment anions with  $n \leq 6$  are produced by nonsequential fission processes after a similar residence time, as suggested by the residence-time measurement.<sup>143</sup> This interpretation is consistent with the results of CID<sup>154</sup> discussed later.

From the results of the velocity measurement of the fragment anions and the above scenario of the fragmentation process, the energy redistribution is analyzed for the translational impact energy to the following kinetic modes: (1) the translational motion of the fragment anion, (2) internal modes of the parent cluster, and (3) those of the surface. The translational energy,  $E_{trans}^{frag}$ , of the fragment cluster anion is evaluated to be about 20% and 10% of the impact energy,  $E_c$ , for  $Al_{11}^-$  and  $Al_7^-$  formation from  $Al_{13}^-$ , respectively; it decreases as the fragment-anion size decreases. The internal energy deposited on the parent cluster anion,  $E_{int}^{cluster}$ , is consumed as kinetic energies of atoms sequentially evaporated,  $E_{trans}^{evap}$ , and dissociation energies of evaporation,  $E_{diss}$ , which is calculated by adding up bond-dissociation energies from the parent-anion size down to the fragment-anion size; it is left as well on a fragment cluster anion,  $E_{int}^{frag}$ , which is presumed almost as much as its bond-dissociation energy. Thus  $E_{int}^{cluster}$  ranges from 20% to 45% of  $E_c$  for the process producing a fragment anion with  $n$  ranging from 11 to 7. Correspondingly, the internal energy of the surface,  $E_{int}^{surface}$ , ranges from 60% to 45% of  $E_c$  as listed in Table 2. It is concluded that most of the impact translational energy is converted to thermal energy. These results suggest that  $Al_N^-$  acquires much energy in its internal modes associated with significant deformation. The metallic bonds prevent  $Al_N^-$  from instantaneous fragmentation to individual atoms (shattering), which is discussed for molecular clusters in section III.4.

III.3.2.b. Impact of Silicon Cluster Anions. Impact of  $Si_N^-$  ( $8 \leq N \leq 12$ ) revealed that  $Si_N^-$  fragments into  $Si_n^-$  with  $n \sim N/2$ , as shown in Figures 13b–f.<sup>155</sup> Dominant fragment anions from  $N = 8–12$  are  $n = 4, n = 5, n = 4, 5,$  and  $6, n = 5,$  and  $n = 6$ , respectively;  $Si_N^-$  seem to produce two fragments with almost the same sizes. On the other hand, impact of  $Al_{13}^-$  shows very broad size-distribution of fragment anions (Figure 13a), which was also true for other sizes  $7 \leq N \leq 25$ .<sup>156</sup> The impact-energy dependence shown for  $Si_{11}^-$  and  $Al_{13}^-$  in Figure 14a indicates clear difference;  $Si_{11}^-$  releases six atoms by about half

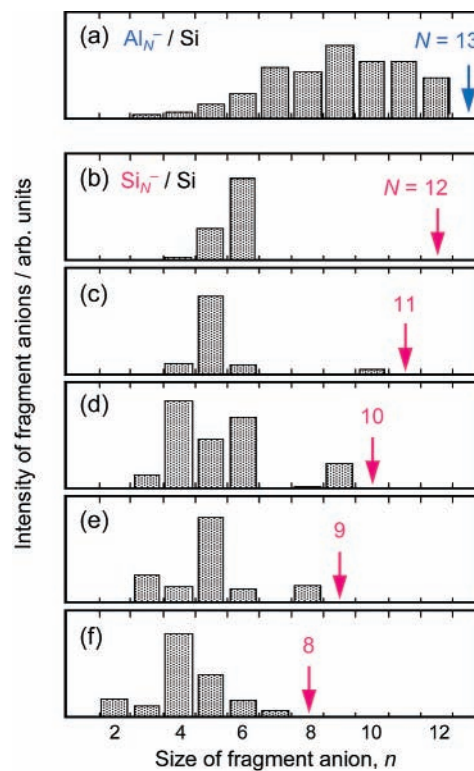


**Figure 13.** Size distributions of fragment anions produced by impact on a silicon surface of (a)  $Al_{13}^-$  at 80 eV and (b)–(f)  $Si_N^-$  ( $N = 12–8$ ) at 50 eV. Arrows show the parent cluster sizes. By the measurements at these impact energies, it is clear that (1)  $Si_N^-$  release more atoms than  $Al_{13}^-$  even at a lower impact energy and (2) larger  $Si_N^-$  release more atoms than smaller ones even with a lower impact energy per atom. These results imply fission processes in  $Si_N^-$  fragmentation.

of the impact energy needed for  $Al_{13}^-$ . These observations suggest a fission process for  $Si_N^-$ . The velocity measurement of the fragment  $Si_5^-$  produced from  $Si_{11}^-$  showed that the normal component is almost conserved,  $v_{r1}/v_{c1} \sim 1$ . A sharp contrast to aluminum cluster anions was observed for the tangential velocity component, Figure 14b;  $v_{t1}/v_{c1}$  is only 0.1 for  $Al_7^-$  produced from  $Al_{13}^-$ , whereas it is as large as 0.5 for  $Si_5^-$  produced from  $Si_{11}^-$ . These results indicate that the impact process of  $Si_N^-$  is much more elastic than that of  $Al_N^-$ . The relatively large tangential velocity is ascribable to a short residence time of  $Si_N^-$  on the surface.

On the basis of these experimental data, it is evaluated that about 40% of the impact energy of  $Si_N^-$  is converted to the translational kinetic energy of the fragments. The internal energy deposited on the parent cluster anion is reported to be about 20% of the impact energy.<sup>152</sup> Therefore, it is estimated that the rest of about 40% goes to the internal energy of the surface, as listed in Table 2.

III.3.2.c. Aluminum vs Silicon Cluster Anions. Overall the difference between aluminum and silicon cluster impact is summarized in Table 2. The major dissociation process of  $Al_N^-$  is sequential evaporation of atoms during a relatively long residence time on the surface, which has an extremely high local temperature at the moment of impact created by a high conversion rate of the impact translational energy to internal energies of the cluster and the surface. The  $Al_N^-$  is so deformable that it accumulates high thermal energy in its internal vibrational modes. On the other hand,  $Si_N^-$  fragments via fission and leaves the surface much more elastically after a short residence time without acquiring high internal energy. These distinct features in the impact dynamics on a silicon surface

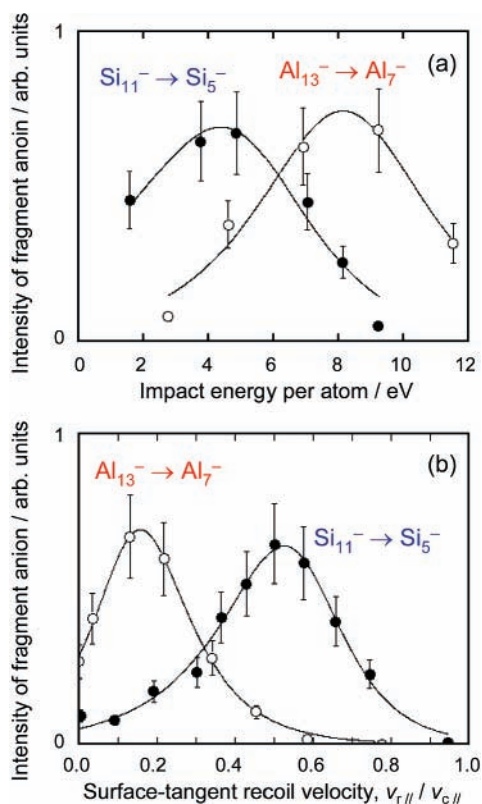


**Figure 14.** Intensities of fragment anions for the processes,  $Al_{13}^- \rightarrow Al_7^-$  (open circles) and  $Si_{11}^- \rightarrow Si_5^-$  (closed circles), upon impact on a silicon surface as a function of (a) the impact energy (per atom) and (b) the normalized surface-tangent recoil velocity,  $v_{H//} / v_{Cl}$ , measured at impact energies of 80 and 50 eV, respectively. The solid curves are guides for the eye.

give explanation for the difference in their reactivity on a graphite surface. The thermal energy of the surface deposited by  $Al_N^-$  is high enough to liberate carbon atoms and the long residence time allows them to react with each other. The effect of the residence time is manifested in the mass spectra shown in Figure 11a, where the intensity ratio of  $Al_nC^-$  to  $Al_n^-$  is larger for smaller  $n$  spending a longer time on the surface. In contrast, the short residence time of  $Si_N^-$  significantly reduces the probability to pickup a liberated surface atoms. These results remind us of bulk properties of aluminum and silicon; aluminum, bound by metallic bonds, has a ductile and malleable nature, whereas silicon, bound by covalent bonds, is hard but brittle. It is worth noting that the bulk mechanical properties are present in the cluster regime with only about ten atoms.

III.3.2.d. Comparison with Photoinduced and Collision-Induced Dissociation. Collisional excitation transfers not only translational energy but also momentum, whereas only electronic energy is deposited upon photoexcitation of an electronic transition. The momentum transfer raises the importance of kinematics as well as energetics. The major difference between atomic and surface collision is that the former often excites a local mode of vibration, whereas the latter is effective for initiating a concerted motion and transfers extremely high energy impulsively at high impinging velocities. Therefore, the three excitation processes, in general, initiate dynamics distinct from each other. These features are illustrated in the following by comparison of the dissociation dynamics of  $Si_N^-$  and  $Al_N^-$  upon surface impact with those initiated by photoabsorption and atomic collision.

For silicon clusters, photodissociation of  $Si_N^-$  ( $9 \leq N \leq 23$ ) has been studied with photon energies in the 2.3–3.5 eV

range.<sup>157</sup> The dissociation proceeded in fission into about half of the original size and the size-distributions of the fragment anions were very similar to the ones obtained in the present surface-impact experiments. This is consistent with the present interpretation that  $Si_N^-$  leaves the surface intact and undergoes fission-type dissociation unimolecularly according to energetics, as concluded also by Whetten and co-workers.<sup>152</sup> The fission-type fragmentation has been observed for positively charged clusters,  $Si_N^+$ , by photodissociation<sup>158,159</sup> and CID<sup>160</sup> experiments as well. Furthermore, similar dissociation processes have been reported for  $Ge_N^\pm$  and  $Sn_N^+$  in photodissociation<sup>157,159</sup> and surface-impact dissociation (SID).<sup>161</sup> The dissociation dynamics does not show clear dependence on excitation processes in these semiconductor clusters bound by covalent bonds.

The dissociation processes of aluminum clusters, on the other hand, are slightly different depending on excitation processes. In photodissociation<sup>18,100,162</sup> and CID,<sup>163,164</sup> cations,  $Al_N^+$  ( $2 \leq N \leq 17$ ), liberate an Al atom (or an  $Al^+$  ion) by statistical mechanism in the excitation-energy range of 2–5 eV. Photodissociation of  $Al_N^-$  ( $2 \leq N \leq 8$ ) is also dominated by an Al atom loss.<sup>162</sup> In CID of  $Al_N^-$  ( $8 \leq N \leq 13$ ) at high collision energies,<sup>154</sup> sequential atom loss is observed down to  $Al_7^-$  without any smaller ones ( $n \leq 6$ ); the statistical dissociation process switches to electron detachment because the electron affinity of  $Al_7^-$  is lower than the bond dissociation energy. The present surface-impact process also proceeds basically according to energetics, but is in contrast to the result of CID in that small fragment anions with  $n \leq 6$  are produced as well; it is ascribable to a nonsequential process specific to the surface-impact excitation, i.e., a dynamical effect leading to fission.

Here we add what is known for silver cluster ions. Dissociation of  $Ag_N^+$  reported for CID ( $3 \leq N \leq 20$ )<sup>165</sup> and SID ( $2 \leq N \leq 4$ )<sup>166</sup> takes place in a statistical manner primarily via sequential atom loss. In contrast, photodissociation of  $Ag_4^+$  described in section II.3.1 exemplifies that dynamics in the excited state dominates the process instead of energetics.

The above comparison illustrates the difference in the dynamics initiated by the three different excitation mechanisms. Clusters excited electronically or vibrationally undergo relaxation most-likely according to energetics in a statistical manner. In this statement, the electronic excitation is assumed to be converted to thermal energy very rapidly because of a high density of internal modes of a cluster. This assumption is not valid in some cases and, thereby, fluorescence or fragmentation on an excited-state potential-energy surface may occur; photoexcitation thus can show nonstatistical relaxation. In the case of collisional excitation by atoms or solid surfaces, the dissociation process may be deviated from a statistical one, particularly when a large-amplitude motion is excited, and is dominated by dynamical factors, in other words, when the rate of such hyperthermal excitation far exceeds those of any thermalization processes. It is noted that the nature of chemical bonds seems to be an important factor in the energetically favored dissociation pathways; the fission-type fragmentation common to clusters of semiconductor elements is contrasted to evaporation of atoms often observed for most of the metal clusters.

**III.4. Surface Impact of Weakly-Bound Molecular Clusters.** In contrast to the aluminum and silicon clusters, weakly bound van-der-Waals clusters exhibit completely different behaviors. In particular, a molecular ion solvated with chemically inert molecules presents an opportunity to investigate dissociation dynamics of the core ion assisted by the solvent via a concerted motion. A clear size effect is expected because

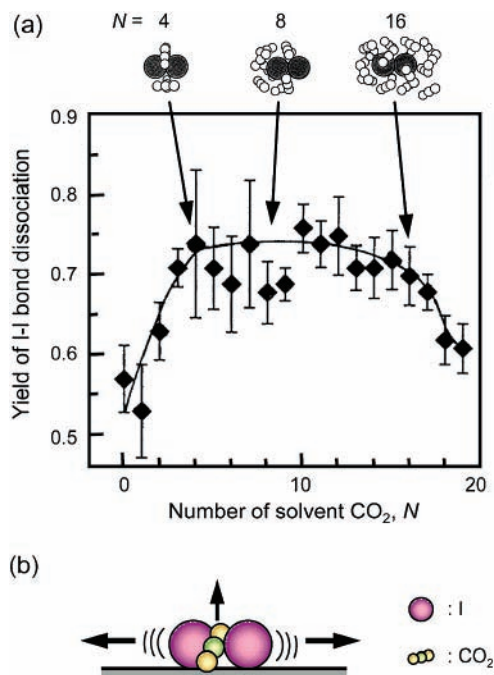


**Figure 15.** (a) Yield of dissociation,  $I_2^- \rightarrow I^-$ , of the core anion as a function of the number of solvent molecules,  $N$ , upon impact of  $I_2^-(CO_2)_N$  on a silicon surface at the impact energy (per  $I_2^-$ ) of 50 eV. The solid curve is a guide for the eye. The inset figures show equilibrium geometries for  $N = 4, 8,$  and  $16$  obtained by MD simulations.<sup>169</sup> (b) Schematic of the “wedge effect,” where a  $CO_2$  molecule splits the I–I bond by a mechanical force.

the spatial arrangement of solvation changes with the number of solvent molecules.

Experiments were performed on solvated molecular anions,  $I_2^-(CO_2)_N$ , impinging on a silicon surface.<sup>167,168</sup> The product anions observed were  $I_2^-$  and  $I^-$  with only a trace amount of  $I_2^-(CO_2)$  and  $I^-(CO_2)$ ; almost all the solvent molecules were blown off and either intact ( $I_2^-$ ) or dissociated ( $I^-$ ) core anion was scattered off. The branching fraction to dissociation of  $I_2^-$  is plotted as a function of the number of solvent molecules in Figure 15a. The following size dependence is discernible; the dissociation yield increases from  $N = 0$  to 4, stays almost constant in  $4 \leq N \leq 15$ , and decreases above  $N = 16$ .

On the basis of the geometrical structures of  $I_2^-(CO_2)_N$  obtained by MD simulations,<sup>169</sup> the size dependence is explained as follows: The decrease in the dissociation yield above  $N = 16$ , is ascribable to recombination of the dissociating  $I_2^-$  by the presence of a solvent cage completed at  $N = 16$ . This “cage effect” was first confirmed in the time-resolved photodissociation experiment; the core anion,  $I_2^-$ , was excited by a picosecond laser pulse to a repulsive potential, which depleted the absorption due to elongation of the I–I bond, and was probed by a second pulse to observe recovery of the absorption.<sup>170,171</sup> The absorption recovered completely within 10 ps in  $I_2^-(CO_2)_{16}$ , but the recovery was not complete for smaller sizes.

On the other hand, the increase in the dissociation yield in the small size range ( $1 \leq N \leq 4$ ) is interpreted as follows: The geometrical structures show that solvent  $CO_2$  molecules are bound in the vicinity of the I–I bond in these sizes. Therefore, one of the  $CO_2$  molecules, which happens to locate between the I–I bond and the surface at the moment of impact, is forced to squeeze in between the iodine atoms and split the I–I bond mechanically as illustrated in Figure 15b, as if a piece of wood is split by an action of a hammer against a wedge (“wedge effect”). As the number of  $CO_2$  molecules that can act as a

wedge increases from  $N = 1$  to 4, the probability of the orientation of the impinging cluster favorable for the wedge effect increases, which raises the dissociation yield of  $I_2^-$ . Further studies by MD simulations showed that about 20% of the impact energy is converted to the vibrational energy of  $I_2^-$  with the presence of a  $CO_2$  molecule, whereas the conversion rate is less than 10% without it.<sup>172</sup> The solvent molecule thus assists the dissociation of the core anion. The “wedge effect” is specific to the surface-impact process exciting a concerted motion of constituent atoms, which does not take place by photoexcitation.

The energy redistribution was studied by the measurements of velocity distributions of recoiling fragment anions. The results showed that they leave the surface after reaching a quasi thermal equilibrium with surface atoms in the impact region; the local temperature was estimated to range between 5000 and 20 000 K at the impact energy of 50 eV (per  $I_2^-$ ) depending on the size and the incidence angle.<sup>173,174</sup> A super-high temperature due to many-body impact was evidenced for molecular clusters as well.

The fragmentation process of the weakly bound clusters, e.g.,  $I_2^-(CO_2)_N$ , is thus much different from that of more rigid metal clusters, e.g.,  $Al_N^-$ . The latter shows a broad size-distribution of fragments as a result of sequential evaporation of atoms, whereas only a core anion is observed without any intermediate sizes in the former. The exclusive production of the core anion is interpreted as “shattering” of the cluster, as explained in Supporting Information S6; a superheated cluster breaks instantaneously into a number of individual molecules in a collective manner, which is a phase transition caused by entropy.<sup>136</sup>

#### IV. A Model Experiment of Cluster Impact Processes: Dynamics of a Liquid Droplet Excited by Multiphoton Absorption at the Surface

**IV.1. Liquid Droplets as a Model of Clusters.** As demonstrated in the preceding section, a cluster exhibits a concerted motion of constituent atoms upon surface-impact excitation. It is of fundamental interest to clarify the temporal evolution of the dissipation processes of the impact energy into internal modes of the cluster and further to kinetic energies of fragments. However, a time-resolved experiment is difficult for the collisional process due to lack of a trigger synchronizing the excitation with a probe. We have developed an experimental technique using a pulsed laser to initiate superheating of the surface of a micrometer-sized liquid droplet, which mimics surface-impact excitation of molecular clusters.

A liquid droplet offers a good model to simulate dynamics of clusters such as collective vibrations, structure deformation, and fragmentation. Excitation of the liquid droplet analogous to surface impact of a cluster is achieved by multiphoton absorption (MPA); a nanosecond mid-IR laser pulse tuned at a vibrational resonance of constituent molecules of the droplet initiates a hyperthermal condition with only surface molecules excited in vibration. Time-resolved images of the excited droplet obtained by a pump–probe technique visualize its energy transport and dissipation dynamics. The results provide evidence for dynamical features such as shock-wave propagation and shattering of the droplet into many pieces of small fragments, which have been predicted for rare-gas clusters by MD simulations illustrating microscopic pictures of surface-impact processes.<sup>133–136</sup>

**IV.2. Experimental Procedures for Mid-Infrared Multiphoton Excitation.** The setup of the present experiment is illustrated in Figure 16. A spherical ethanol droplet of a 70- $\mu$ m

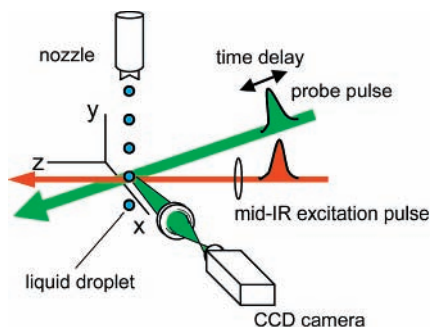


**Figure 16.** Schematics of the experimental setup for time-resolved imaging of dynamics of a liquid droplet following surface excitation by mid-IR MPA.

diameter (3 nmol) was produced by a microdroplet generator (microdrop GmbH) in the air through a pulsed nozzle operated by a piezo-electric transducer. Although the present experiment was performed in the atmospheric environment, techniques have been developed to introduce the droplet even into a vacuum.<sup>175,176</sup> Excitation of the droplet was initiated by a 10-ns laser pulse, at the wavelength of 2.96  $\mu\text{m}$  and with the pulse energy of 1–8 mJ, generated by an optical parametric oscillator/amplifier system based on  $\text{LiNbO}_3$  crystals (Model 4-100, INRAD) pumped by a fundamental output of a Q-switched Nd:YAG laser (GCR-150, Spectra Physics). The spot size of the mid-IR pulse at the droplet was adjusted to 500  $\mu\text{m}$  in diameter; therefore, about 2% of the pulse energy was incident on the droplet. The wavelength was resonant so strongly with the O–H vibrational mode of liquid ethanol (linear absorption coefficient,  $\alpha \approx 1200 \text{ cm}^{-1}$ ) that more than 90% of the incident energy was absorbed within 20  $\mu\text{m}$  beneath the surface of the droplet. Note that 3-nmol liquid ethanol at room temperature requires 0.02 mJ for the entire volume to be heated to the boiling temperature (78  $^\circ\text{C}$ ) and an additional 0.12 mJ to be further transferred to the vapor phase. The excited droplet was probed by a visible laser pulse (second harmonics of a second Q-switched Nd:YAG laser at 532 nm attenuated to 50  $\mu\text{J}$  with a 5-mm spot size) illuminated almost collinearly (about  $10^\circ$ ) with respect to the mid-IR excitation beam after a variable time delay with a 10-ns resolution. A spatial image of the probe light scattered from the droplet was detected by a CCD camera located at the right angle with respect to the mid-IR laser beam. The spatial resolution of the image was 6  $\mu\text{m}/\text{pixel}$ . As the droplet was transparent at the probe wavelength, the image of the scattered probe light visualized discontinuity in the refractive index not only at the surface of the droplet but also in the interior region locally modulated in density (e.g., by heating). The CCD image was transferred to a personal computer through an 8-bit image acquisition card. All the electronics were synchronized with a video signal of the CCD camera by a homemade electric circuit.

**IV.3. Energy Dissipation Processes.** Figure 17 shows a series of droplet images as a function of time, where the droplet was excited by an 8.0-mJ ( $4.0 \text{ J cm}^{-2}$ ) pulse irradiated from the right-hand side. The color indicates the intensity of the scattered probe light calibrated by the bar graph in the inset. Figure 17a is an image at a negative delay showing an original droplet without excitation. Two bright spots are due to two optical paths allowed for the spherical droplet that reflect the probe laser beam by almost right angle. The distance between the two spots is about  $0.9d$ , where  $d$  represents the diameter of the droplet. Figures 17b–e show images at 0.1, 1, 2, and 10  $\mu\text{s}$ , respectively, after excitation.

The dynamics of the excited droplet is characterized by the following five steps: (1) Ethanol molecules evaporate from the

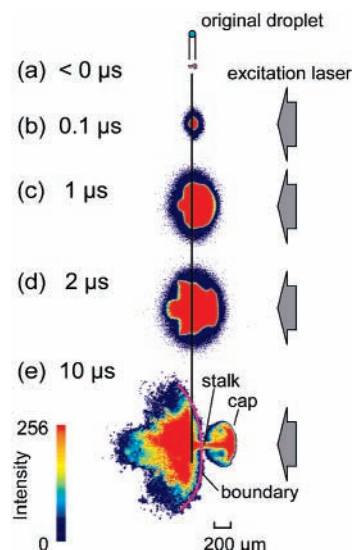


**Figure 17.** Time-resolved CCD images of an exploding ethanol droplet ( $\phi$  70  $\mu\text{m}$ ) at several time delays between the 2.96  $\mu\text{m}$  excitation laser pulse of 8.0 mJ ( $4.0 \text{ J cm}^{-2}$ ), irradiated from the right-hand side as shown by arrows, and the 532 nm probe pulse. The color indicates the intensity of the scattered probe light calibrated by the bar graph in the inset. The detector is saturated in the red region. An image at a negative delay, (a), shows an original droplet without excitation. Other images are at (b) 0.1, (c) 1, (d) 2, and (e) 10  $\mu\text{s}$  after excitation.

surface as discernible by the outer ellipsoidal regions (dark blue) in Figures 17b–d. Their velocities are estimated to be  $740 \pm 120$ ,  $950 \pm 340$ , and  $1290 \pm 320 \text{ m s}^{-1}$ , respectively, for forward (emitted to the downstream of the excitation laser (the left-hand side)), backward (to upstream (the right-hand side)), and sideward components. The thermal velocity of the evaporating molecules is equivalent to a local temperature of about 3000 K in the excited region. (2) The droplet is deformed in such a manner that it is compressed along the axis of the excitation laser beam, as shown by the contour of the central red part of Figure 17b. (3) At 1  $\mu\text{s}$ , a hemispherical expansion is discernible in the backward side with a dull contour edge. There appears nonspherical distortion in the forward side. (4) At 2  $\mu\text{s}$ , the contour edge in the backward side turns to be sharp, which is a precursor of a jet-like plume emerging later. The forward structure grows into three wings. (5) At 10  $\mu\text{s}$ , a jet-like plume of a dense ethanol gas is launched backward, which has a mushroom-like shape with a front-end cap and a trailing stalk. The mushroom pattern is a basic structure often observed in turbulent flows.<sup>177</sup> The velocity of the front edge of the cap structure is measured to be  $39 \pm 3 \text{ m s}^{-1}$ . The diameter of the columnar stalk is about 70  $\mu\text{m}$ , which is the same as the size of the original droplet. In the forward side, in contrast, a number of small secondary droplets (“splash”) is emitted to spatially dispersed directions, of which the sizes are several micrometers or less as discernible by the small blue dots. There is a clear boundary between the forward and the backward regions; no splash is observed in the backward side. At delays longer than 10  $\mu\text{s}$ , the growth of the pattern is essentially proportional to the elapsed time and the disintegrated droplet vanishes finally via evaporation of ethanol molecules.

The destiny of the droplet is critically dependent on the incident pulse energy as shown in Figure 18a, images at 10  $\mu\text{s}$  after excitation. At low excitation energies (0.5 and 1.5  $\text{J cm}^{-2}$ ), vapor and very small droplets of ethanol are ejected only backward, whereas the main body of the droplet remains intact. The backward ejection is analogous to the formation of a vapor layer in the Leidenfrost phenomenon of a liquid droplet on a

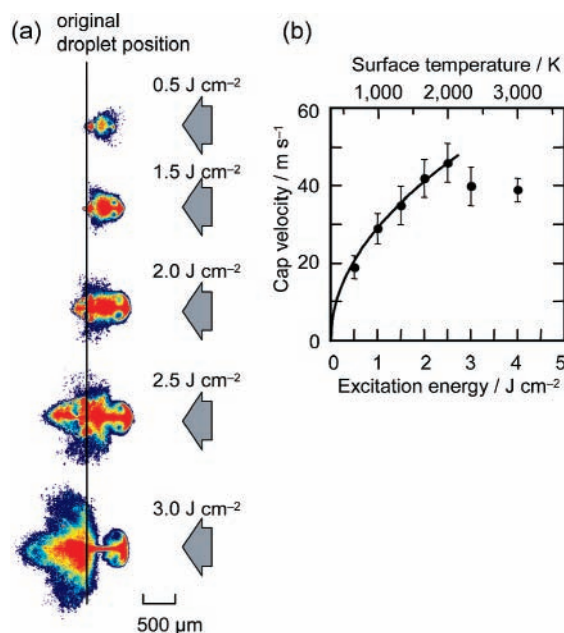


**Figure 18.** (a) Images of the droplet at  $10 \mu\text{s}$  after excitation as a function of the intensity of the excitation laser at  $2.96 \mu\text{m}$ . The laser pulse is illuminated from the right-hand side as shown by arrows. The vertical solid line shows the original position of the droplet. See Figure 17 for the color-to-intensity calibration. (b) Velocity of the front edge of the cap structure (cap velocity) as a function of the intensity of the mid-IR excitation pulse. The excitation intensity is converted to the local temperature of the illuminated surface as shown by the top axis. The solid curve indicates the square-root dependence on the excitation intensity, which explains the behavior below  $2.5 \text{ J cm}^{-2}$ .

hot pan,<sup>131,132</sup> the momenta of the ejected vapor and very small secondary droplets make the droplet float. As the excitation energy increases to  $2.5 \text{ J cm}^{-2}$ , the cap structure of the backward plume becomes clear and the body gains an excess energy for nearly isotropic fragmentation. Finally, at  $3.0 \text{ J cm}^{-2}$ , the droplet body is disintegrated into a pattern having a completely anisotropic structure similar to that observed at  $4.0 \text{ J cm}^{-2}$  (Figure 17e).

A sudden change in the process in the vicinity of  $3.0 \text{ J cm}^{-2}$  is illustrated in Figure 18b, where the velocity of the front edge of the cap structure is plotted as a function of the excitation energy. As the excitation energy increases, the velocity increases proportionally to the square-root of the excitation energy until the threshold energy of  $2.5 \text{ J cm}^{-2}$ ; this result indicates that the energy deposited on the droplet is converted to translational energy of the plume at a constant conversion rate. On the other hand, the increase in the velocity suddenly drops and levels off above the threshold; the droplet body rebounds the plume less efficiently and the translational energy is converted to that of the forward splash instead. The local temperature of the surface at the threshold energy is  $2200 \pm 200 \text{ K}$ , corresponding to a thermal velocity of  $1090 \pm 50 \text{ m s}^{-1}$ . The velocity is approximately the same as the velocity of sound in liquid ethanol ( $1134 \text{ m s}^{-1}$  at  $30 \text{ }^\circ\text{C}$ ). This fact implies that a supersonic shock wave is generated above the threshold. The hydrogen-bond network of liquid ethanol is destroyed by the shock wave to cause extensive disintegration of the droplet body into splash.

The evidence for the shock wave is given in Figure 19. At the excitation energy above the threshold (Figure 19a), an increase in the scattered light intensity at the illuminated side in the early stages ( $10\text{--}20 \text{ ns}$ ) is followed by a successive brightening of the forward side ( $30\text{--}50 \text{ ns}$ ). This brightening, i.e., discontinuity in the refractive index, travels at the velocity

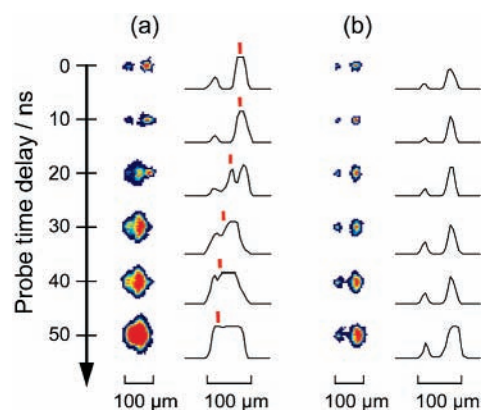


**Figure 19.** Images of the droplet at early time delays. The mid-IR laser pulse is illuminated from the right-hand side. The excitation energies are (a)  $3.0$  and (b)  $1.0 \text{ J cm}^{-2}$ . The solid lines show the horizontal cross section of the image intensity across the equator of the droplet. The red bars in (a) show a shock-wave front traveling at  $1300 \pm 200 \text{ m s}^{-1}$ . It is not discernible in (b); the intensity at the illuminated side grows rapidly, whereas the other side gains the intensity only slightly without any shock-wave propagation across the droplet.

of  $1300 \pm 200 \text{ m s}^{-1}$ , giving a picture of a shock wave. In contrast, images obtained below the threshold (Figure 19b) exhibit no indication of such a behavior; heat deposited on the illuminated side diffuses much more slowly across the droplet.

In conclusion, excitation of an ethanol droplet by MPA of mid-IR light, an analogue of molecular-cluster impact, identified two shattering processes: (1) backward plume ejection from a superheated droplet surface (statistical shattering), which is a liquid–gas-type phase transition driven by a preference for an increase in entropy,<sup>136</sup> and (2) disintegration of the rest of the droplet body into dispersed forward splash due to a shock wave (dynamical shattering), which causes ballistic hydrogen-bond breaking. The shock wave is initiated by shakeup of ethanol molecules above a critical temperature of about  $2200 \text{ K}$ , where the thermal velocity is about  $1100 \text{ m s}^{-1}$ . It is noted here that, when the excitation laser pulse is off-resonance from the absorption, the droplet is disintegrated in a totally different scenario because the laser pulse penetrates inside.<sup>178</sup> The dynamical processes, i.e., shattering and a shock wave, predicted by MD simulations of surface impact of rare-gas clusters were thus observed by the present model experiment.

## V. Summary and Outlook

Upon photoexcitation of an electronic state, the electronic energy is most-likely converted to vibrational energies of internal modes (thermal energy) of a cluster. This leads to unimolecular dissociation proceeding in a statistical manner; bond dissociation energies are determined as described for  $\text{Mn}_N^+$  ( $N \leq 7$ ). If the dissociation is completed within the experimental time scale, the dissociation yield as a function of the photon energy gives an optical absorption spectrum. Photodissociation/photodepletion spectroscopy is currently the most powerful technique of absorption spectroscopy applicable to size-selected cluster ions. The spectra provide materials properties of clusters with the aid of ab initio calculations. It was highlighted that  $\text{Mn}_2^+$  and  $\text{Mn}_3^+$  show ferromagnetic coupling between local spins, which is in striking contrast to antiferromagnetic bulk manganese.

Contrasted dynamics was found for  $\text{Ag}_4^+$ , which dissociates in a nonstatistical manner on a potential-energy surface of the excited state. This finding may be related to emissivity of silver clusters in an argon matrix,<sup>20–23</sup> where the clusters are prevented from dissociation and stay in the excited electronic state until

they fluoresce ( $\sim 1$  ns). These behaviors are different from a surface-plasmon resonance reported for  $\text{Ag}_N^+$  in previous studies.<sup>93–95</sup> The former represents a single-electron transition between molecular orbitals, whereas the latter is collective excitation of electrons described by the jellium model, where valence electrons are assumed to be confined in a potential well formed by ionic cores of constituent atoms. A possible reason explaining this difference is the temperature of the clusters studied; cold in the former, whereas hot in the latter. These results suggest that thermal motions may play a role in the evolution of metallic properties as well as the size.

To obtain electronic structures in high resolution, a “direct” method for absorption measurement should be developed for a free cluster, without relying on dissociation; the resolution may be lowered by the lifetime broadening in photodissociation. For high-sensitivity absorption measurements, cavity ring-down spectroscopy<sup>179</sup> (or photon-trap spectroscopy<sup>180</sup> for generality) is promising; a lifetime of photons trapped in an optical cavity is measured to obtain an absorption cross section of a sample filled in the cavity. Although this technique has been applied to several metal clusters generated in a supersonic jet,<sup>181–184</sup> the size of the detectable cluster is limited so far only to dimers and trimers because of the lower density of larger clusters. We are currently developing an experimental scheme combining the high-sensitivity spectroscopy with a cluster-storage technique using an ion trap. Absorption spectra have been measured for atomic ions of manganese trapped at a density over  $10^7 \text{ cm}^{-3}$  in a 40-cm long rf trap temperature-controlled to 10 K; the resolution is high enough for hyperfine structures.<sup>185</sup> This technique is applicable as well to matrix-isolated or supported clusters on a solid substrate.<sup>180,186–188</sup> High-resolution spectroscopy under controlled temperatures is needed to gain deeper insights into the problems of vibronic coupling, e.g., the transition from the molecular picture to the jellium model. This novel technique would contribute to the next stage of cluster spectroscopy.

Cluster impact on a solid surface has been shown to create extraordinary conditions for chemistry. (1) An extremely high temperature is achieved by efficient and rapid deposition of translational energy via many-body collisions, as revealed by energy-redistribution process upon impact of  $\text{Al}_N^-$  ( $8 \leq N \leq 13$ ). The dissociation process is distinguished from those of photodissociation and CID proceeding via statistical mechanisms. (2) The high-temperature environment promotes a specific chemical reaction, as exemplified by selective formation of a pickup product,  $\text{Al}_7\text{C}^-$ , upon impact on graphite. (3) The impact of  $\text{Al}_N^-$  is contrasted to that of  $\text{Si}_N^-$ ; the former is heavily inelastic, whereas the latter is more elastic. This contrast is similar to that in the bulk properties, i.e., ductile aluminum vs brittle silicon, indicating a close relationship between the nature of the chemical bond and the dynamics observed. (4) A specific-reaction mode is excited by an impulsive force; the wedge effect in  $\text{I}_2^-(\text{CO}_2)_N$ , where the I–I bond is split mechanically by a thrust action of a solvent  $\text{CO}_2$  molecule. The solvent  $\text{CO}_2$  cluster, on the other hand, undergoes shattering into individual monomers. These studies create a new field of chemistry, namely, cluster-impact chemistry, which utilizes synergic processes of constituent atoms and molecules.

A further experiment was performed on a liquid droplet, which initiates, time-resolves, and visualizes energy-dissipation processes modeling those in the surface impact of molecular clusters, by MPA of a mid-IR laser pulse. Two characteristic processes were identified: (1) The superheated surface molecules are ejected into the gas phase (statistical shattering) and

(2) a shock wave of energy flow generated by the superheated surface disintegrates the entire droplet ballistically (dynamical shattering). Moreover, the mid-IR multiphoton excitation of a liquid provides novel opportunities for chemistry of liquid-phase molecules as well, in particular, by combination with mass spectrometry of ejected species; for example, high-temperature water chemistry<sup>189</sup> and a probe of the local structure of hydrogen bonding.<sup>190</sup> It has even been applied to isolate nonvolatile molecules of biological interest as solvated clusters from solution, for studies of structures and reactivities.<sup>175,191–193</sup>

Finally, we mention that one of the important issues to be challenged is thermodynamics such as freezing, melting, and boiling of clusters. Haberland and co-workers have pioneered this research for  $\text{Na}_N^+$ ;<sup>194</sup> they obtained size-dependent features in the phase transition based on the measurements of caloric curves (internal energy vs temperature) by developing techniques of temperature control by buffer-gas collision and an internal-energy measurement by photofragment-mass analysis. Unfortunately, the technique is not applicable to other clusters because it relies on the property specific to sodium clusters. Therefore, a more general technique is needed, particularly a thermometer with wide applicability. For free clusters, one possibility might be the measurement of the spectrum of “blackbody” radiation (clusters are so small that they might not be “black” in reality). Such measurements have been reported for clusters of refractory metals<sup>195,196</sup> and  $\text{C}_{60}$ <sup>197</sup> above 3000 K, where strong radiation is observed in the visible range; the radiative cooling may even compete with dissociation in such a highly excited cluster.<sup>198</sup> However, one needs a completely new detection scheme for low-temperature measurements, because the spectrum shifts down even to the far-IR range and becomes considerably weaker. For clusters impacting on a solid surface, scattered clusters highly excited in vibration might emit light, which should reflect the temperature created upon impact.<sup>199</sup> Not only thermodynamics but also many other open questions are to be investigated in cluster dynamics to bridge the macroscopic and microscopic knowledge in chemistry.

**Acknowledgment.** I thank Professor T. Kondow for his support and encouragement throughout the present work. I am grateful to Professors H. Yasumatsu, who is the co-worker in the surface-impact experiments as well, and M. Ichihashi for stimulating daily discussion. Thanks are also due to Drs. H. Yoshida, S. Minemoto, K. Tono, A. Matsushita, M. Kulawik, T. Majima, and K. Egashira and Ms. M. Iseda for collaboration in the laser spectroscopy and Professors M. Tsukada, H. Imoto, and Y. Kawazoe and Dr. T. M. Briere in ab initio calculations. The support for the surface-impact experiments by Professors M. Takami and K. Kaya, and the stimulating discussion with Professors V. Bonačić-Koutecký, on the structures and dynamics of metal clusters, and R. D. Levine, on the surface-impact processes, are gratefully acknowledged. I am thankful to Professor J. M. Lisy for critical comments on the manuscript. The present work was supported by the Special Cluster Research Project of Genesis Research Institute, Inc., and by the Meso-phase Chemistry Project of RIKEN.

**Supporting Information Available:** PDF file containing (1) text and Figure S1 providing the time scale of predissociation; (2) text supplementary to the study of photodissociation dynamics of  $\text{Ag}_4^+$ ; (3) text describing procedures of simulation for absorption spectra of  $\text{Mn}_{2,3}^+$ ; (4) text describing collective motions excited by atomic collision; (5) text describing procedures for recoil-velocity measurement in the  $\text{Al}_N^-$ -impact

experiment; (6) text describing the shattering process of molecular clusters. This material is available free of charge via the Internet at <http://pubs.acs.org>.

## References and Notes

- (1) Kubo, R. *J. Phys. Soc. Jpn.* **1962**, *17*, 975.
- (2) Koutecký, J.; Fantucci, P. *Chem. Rev.* **1986**, *86*, 539.
- (3) Morse, M. D. *Chem. Rev.* **1986**, *86*, 1049.
- (4) de Heer, W. A. *Rev. Mod. Phys.* **1993**, *65*, 611.
- (5) Brack, M. *Rev. Mod. Phys.* **1993**, *65*, 677.
- (6) Haberland, H. *Clusters of Atoms and Molecules I: Theory, Experiment, and Clusters of Atoms; II: Solvation and Chemistry of Free Clusters, and Embedded, Supported and Compressed Clusters*; Springer-Verlag: Berlin, 1994.
- (7) Kreibig, U.; Vollmer, M. *Optical Properties of Metal Clusters*; Springer-Verlag: Berlin, 1995.
- (8) Kondow, T.; Kaya, K.; Terasaki, A. *Structures and Dynamics of Clusters*; Universal Academy Press, Inc.: Tokyo, 1996.
- (9) Sugano, S.; Koizumi, H. *Microcluster Physics*, 2nd ed.; Springer-Verlag: Berlin, 1998.
- (10) Meiwes-Broer, K. H. *Metal Clusters at Surfaces: Structure, Quantum Properties, Physical Chemistry*; Springer-Verlag: Berlin, 2000.
- (11) Alonso, J. A. *Chem. Rev.* **2000**, *100*, 637.
- (12) Campbell, E. E. B.; Larsson, M. *The Physics and Chemistry of Clusters*, Proceedings of Nobel Symposium 117; World Scientific Publishing: Singapore, 2001.
- (13) Kondow, T.; Mafuné, F. *Progress in Experimental and Theoretical Studies of Clusters*; Advanced Series in Physical Chemistry 13; World Scientific Publishing: Singapore, 2003.
- (14) Solov'yov, A.; Connerade, J.-P. *Latest Advances in Atomic Cluster Collisions: Fission, Fusion, Electron, Ion and Photon Impact*; Imperial College Press: London, 2004.
- (15) Cluster Chemistry and Dynamics Special Feature. *Proc. Natl. Acad. Sci. U.S.A.* **2006**, *103*, 10552.
- (16) Bréchnignac, C.; Cahuzac, Ph.; Leygnier, J.; Weiner, J. *J. Chem. Phys.* **1989**, *90*, 1492.
- (17) Bréchnignac, C.; Busch, H.; Cahuzac, Ph.; Leygnier, J. *J. Chem. Phys.* **1994**, *101*, 6992.
- (18) Ray, U.; Jarold, M. F.; Bower, J. E.; Kraus, J. S. *J. Chem. Phys.* **1989**, *91*, 2912.
- (19) Hild, U.; Dietrich, G.; Krückeberg, S.; Lindinger, M.; Lützenkirchen, K.; Schweikhard, L.; Walther, C.; Ziegler, J. *Phys. Rev. A* **1998**, *57*, 2786.
- (20) Félix, C.; Sieber, C.; Harbich, W.; Buttet, J.; Rabin, I.; Schulze, W.; Ertl, G. *Chem. Phys. Lett.* **1999**, *313*, 105.
- (21) Rabin, I.; Schulze, W.; Ertl, G.; Félix, C.; Sieber, C.; Harbich, W.; Buttet, J. *Chem. Phys. Lett.* **2000**, *320*, 59.
- (22) Félix, C.; Sieber, C.; Harbich, W.; Buttet, J.; Rabin, I.; Schulze, W.; Ertl, G. *Phys. Rev. Lett.* **2001**, *86*, 2992.
- (23) Sieber, C.; Buttet, J.; Harbich, W.; Félix, C.; Mitrić, R.; Bonačić-Koutecký, V. *Phys. Rev. A* **2004**, *70*, 041201(R).
- (24) Armentrout, P. B. Threshold collision-induced dissociations for the determination of accurate gas-phase binding energies and reaction barriers. In *Modern Mass Spectrometry*; Topics in Current Chemistry No. 225; Springer-Verlag: Berlin, 2003; p 233.
- (25) Ozaki, Y.; Ichihashi, M.; Kondow, T. *Chem. Phys. Lett.* **1991**, *182*, 57.
- (26) Ozaki, Y.; Ichihashi, M.; Kondow, T. *Chem. Phys. Lett.* **1992**, *188*, 555.
- (27) Buck, U.; Krohne, R. *Phys. Rev. Lett.* **1994**, *73*, 947.
- (28) Buck, U.; Krohne, R.; Lohbrandt, P. *J. Chem. Phys.* **1997**, *106*, 3205.
- (29) Nonose, S.; Tanaka, H.; Mizuno, T.; Hirokawa, J.; Kondow, T. *J. Chem. Phys.* **1996**, *104*, 5869.
- (30) Nonose, S.; Tanaka, H.; Mizuno, T.; Kim, N. J.; Someda, K.; Kondow, T. *J. Chem. Phys.* **1996**, *105*, 9167.
- (31) Hertel, I. V.; Schulz, C. P.; Goerke, A.; Palm, H.; Leipelt, G. *J. Chem. Phys.* **1997**, *107*, 3528.
- (32) Yasumatsu, H.; Kondow, T. *Rep. Prog. Phys.* **2003**, *66*, 1783.
- (33) Raz, T.; Levine, R. D. *J. Am. Chem. Soc.* **1994**, *116*, 1167.
- (34) Amrein, A.; Simpson, R.; Hackett, P. *J. Chem. Phys.* **1991**, *95*, 1781.
- (35) Herrmann, A.; Hofmann, M.; Leutwyler, S.; Schumacher, E.; Wöste, L. *Chem. Phys. Lett.* **1979**, *62*, 216.
- (36) Morse, M. D.; Hopkins, J. B.; Langridge-Smith, P. R. R.; Smalley, R. E. *J. Chem. Phys.* **1983**, *79*, 5316.
- (37) Bondybey, V. E.; English, J. H. *J. Chem. Phys.* **1981**, *74*, 6978.
- (38) Crumley, W. H.; Hayden, J. S.; Gole, J. L. *J. Chem. Phys.* **1986**, *84*, 5250.
- (39) Rohlfling, E. A.; Valentini, J. *J. Chem. Phys. Lett.* **1986**, *126*, 113.
- (40) Brucat, P. J.; Zheng, L.-S.; Pettiette, C. L.; Yang, S.; Smalley, R. E. *J. Chem. Phys.* **1986**, *84*, 3078.
- (41) Menezes, W. J. C.; Knickelbein, M. B. *J. Chem. Phys.* **1993**, *98*, 1856.
- (42) Posey, L. A.; Deluca, M. J.; Johnson, M. A. *Chem. Phys. Lett.* **1986**, *131*, 170.
- (43) Cheshnovsky, O.; Yang, S. H.; Pettiette, C. L.; Craycraft, M. J.; Smalley, R. E. *Rev. Sci. Instrum.* **1987**, *58*, 2131.
- (44) Wolf, S.; Sommerer, G.; Rutz, S.; Schreiber, E.; Leisner, T.; Wöste, L.; Berry, R. S. *Phys. Rev. Lett.* **1995**, *74*, 4177.
- (45) Ashfold, M. R.; Lambert, I. R.; Mordaunt, D. H.; Morley, G. P.; Western, C. M. *J. Phys. Chem.* **1992**, *96*, 2938.
- (46) Nagata, T.; Kondow, T. *J. Chem. Phys.* **1993**, *98*, 290.
- (47) Brehm, B.; Gusinow, M. A.; Hall, J. L. *Phys. Rev. Lett.* **1967**, *19*, 737.
- (48) Siegel, M. W.; Celotta, R. J.; Hall, J. L.; Levine, J.; Bennett, R. A. *Phys. Rev. A* **1972**, *6*, 607.
- (49) Kruit, P.; Read, F. H. *J. Phys. E* **1983**, *16*, 313.
- (50) Yoshida, H.; Terasaki, A.; Kobayashi, K.; Tsukada, M.; Kondow, T. *J. Chem. Phys.* **1995**, *102*, 5960.
- (51) Baguenard, B.; Wills, J. B.; Pagliarulo, F.; Lépine, F.; Climen, B.; Barbaire, M.; Clavier, C.; Lebeault, M. A.; Bordas, C. *Rev. Sci. Instrum.* **2004**, *75*, 324 and references therein.
- (52) Iseda, M.; Nishio, T.; Han, S. Y.; Yoshida, H.; Terasaki, A.; Kondow, T. *J. Chem. Phys.* **1997**, *106*, 2182.
- (53) Slater, J. C. *The Calculation of Molecular Orbitals*; Wiley: New York, 1979.
- (54) Averill, F. W.; Ellis, D. E. *J. Chem. Phys.* **1973**, *59*, 6412.
- (55) Rosén, A.; Ellis, D. E.; Adachi, H.; Averill, F. W. *J. Chem. Phys.* **1976**, *65*, 3629.
- (56) Adachi, H.; Tsukada, M.; Satoko, C. *J. Phys. Soc. Jpn.* **1978**, *45*, 875.
- (57) Adachi, H.; Shiokawa, S.; Tsukada, M.; Satoko, C.; Sugano, S. *J. Phys. Soc. Jpn.* **1979**, *47*, 1528.
- (58) Imoto, H.; Saito, T.; Adachi, H. *Inorg. Chem.* **1995**, *34*, 2415.
- (59) Bonačić-Koutecký, V.; Češpiva, L.; Fantucci, P.; Pittner, J.; Koutecký, J. *J. Chem. Phys.* **1994**, *100*, 490.
- (60) Massobrio, C.; Pasquarello, A.; Car, R. *Phys. Rev. Lett.* **1995**, *75*, 2104.
- (61) Grönbeck, H.; Rosén, A. *J. Chem. Phys.* **1997**, *107*, 10620.
- (62) Fan, H.-J.; Liu, C.-W.; Liao, M.-S. *Chem. Phys. Lett.* **1997**, *273*, 353.
- (63) Fournier, R.; Pang, T.; Chen, C. *Phys. Rev. A* **1998**, *57*, 3683.
- (64) Wu, X.; Ray, A. K. *J. Chem. Phys.* **1999**, *110*, 2437.
- (65) Li, S.; Alemany, M. M. G.; Chelikowsky, J. R. *J. Chem. Phys.* **2004**, *121*, 5893.
- (66) Tono, K.; Terasaki, A.; Ohta, T.; Kondow, T. *Phys. Rev. Lett.* **2003**, *90*, 133402.
- (67) Tono, K.; Terasaki, A.; Ohta, T.; Kondow, T. *J. Chem. Phys.* **2003**, *119*, 11221.
- (68) Weber, S. E.; Reddy, B. V.; Rao, B. K.; Jena, P. *Chem. Phys. Lett.* **1998**, *295*, 175.
- (69) Reddy, B. V.; Khanna, S. N. *Phys. Rev. Lett.* **1999**, *83*, 3170.
- (70) Reddy, B. V.; Khanna, S. N.; Ashman, C. *Phys. Rev. B* **2000**, *61*, 5797.
- (71) Knickelbein, M. B.; Menezes, W. J. C. *Phys. Rev. Lett.* **1992**, *69*, 1046.
- (72) Collings, B. A.; Athanassenas, K.; Lacombe, D.; Rayner, D. M.; Hackett, P. A. *J. Chem. Phys.* **1994**, *101*, 3506.
- (73) Collings, B. A.; Athanassenas, K.; Rayner, D. M.; Hackett, P. A. *Chem. Phys. Lett.* **1994**, *227*, 490.
- (74) Minemoto, S.; Terasaki, A.; Kondow, T. *J. Chem. Phys.* **1996**, *104*, 5770.
- (75) Ayotte, P.; Bailey, C. G.; Kim, J.; Johnson, M. A. *J. Chem. Phys.* **1998**, *108*, 444.
- (76) Knickelbein, M. B. *J. Chem. Phys.* **1994**, *100*, 4729.
- (77) Broyer, M.; Delacrétaz, G.; Labastie, P.; Wolf, J. P.; Wöste, L. *Phys. Rev. Lett.* **1986**, *57*, 1851.
- (78) de Heer, W. A.; Selby, K.; Kresin, V.; Masui, J.; Vollmer, M.; Châtelain, A.; Knight, W. D. *Phys. Rev. Lett.* **1987**, *59*, 1805.
- (79) Minemoto, S.; Terasaki, A.; Imoto, H.; Kondow, T. *J. Chem. Phys.* **1998**, *109*, 9737.
- (80) Terasaki, A.; Minemoto, S.; Iseda, M.; Kondow, T. *Eur. Phys. J. D* **1999**, *9*, 163.
- (81) Dietz, T. G.; Duncan, M. A.; Powers, D. E.; Smalley, R. E. *J. Chem. Phys.* **1981**, *74*, 6511.
- (82) Su, C.-X.; Hales, D. A.; Armentrout, P. B. *J. Chem. Phys.* **1994**, *99*, 6613.
- (83) Minemoto, S.; Takahashi, K.; Matsumoto, J.; Iseda, M.; Terasaki, A.; Imoto, H.; Kondow, T. *Z. Phys. D* **1997**, *40*, 13.
- (84) Minemoto, S.; Terasaki, A.; Kondow, T. *J. Electron Spectros. Relat. Phenom.* **2000**, *106*, 171.

- (85) Martínez, J. I.; Castro, A.; Rubio, A.; Alonso, J. A. *J. Comput. Theor. Nanosci.* **2006**, *3*, 761.
- (86) Antonietti, J. M.; Châtelain, A.; Fedrigo, S. *J. Chem. Phys.* **2001**, *114*, 2981.
- (87) Fielicke, A.; Kirilyuk, A.; Ratsch, C.; Behler, J.; Scheffler, M.; von Helden, G.; Meijer, G. *Phys. Rev. Lett.* **2004**, *93*, 023401.
- (88) Ratsch, C.; Fielicke, A.; Kirilyuk, A.; Behler, J.; von Helden, G.; Meijer, G.; Scheffler, M. *J. Chem. Phys.* **2005**, *122*, 124302.
- (89) Bonačić-Koutecký, V.; Češpiva, L.; Fantucci, P.; Koutecký, J. *J. Chem. Phys.* **1993**, *98*, 7981.
- (90) Rayner, D. M.; Athanassenas, K.; Collings, B. A.; Mitchell, S. A.; Hackett, P. A. Silver clusters and silver cluster/ammonia complexes. In *Theory of atomic and molecular clusters*; Jellinek, J., Ed.; Springer-Verlag: Berlin, 1999; p 371.
- (91) Schooss, D.; Gilb, S.; Kaller, J.; Kappes, M. M.; Furche, F.; Köhn, A.; May, K.; Ahlrichs, R. *J. Chem. Phys.* **2000**, *113*, 5361 and 10413.
- (92) Bonačić-Koutecký, V.; Pittner, J.; Boiron, M.; Fantucci, P. *J. Chem. Phys.* **1999**, *110*, 3876.
- (93) Tiggesbäumker, J.; Köller, L.; Lutz, H. O.; Meiwes-Broer, K.-H. *Chem. Phys. Lett.* **1992**, *190*, 42.
- (94) Tiggesbäumker, J.; Köller, L.; Meiwes-Broer, K.-H.; Liebsch, A. *Phys. Rev. A* **1993**, *48*, R1749.
- (95) Tiggesbäumker, J.; Köller, L.; Meiwes-Broer, K.-H. *Chem. Phys. Lett.* **1996**, *260*, 428.
- (96) Federmann, F.; Hoffmann, K.; Quaas, N.; Toennies, J. P. *Eur. Phys. J. D* **1999**, *9*, 11.
- (97) Bonačić-Koutecký, V.; Veyret, V.; Mitrić, R. *J. Chem. Phys.* **2001**, *115*, 10450.
- (98) Ellert, C.; Schmidt, M.; Schmitt, C.; Reiners, T.; Haberland, H. *Phys. Rev. Lett.* **1995**, *75*, 1731.
- (99) Schmidt, M.; Ellert, C.; Kronmüller, W.; Haberland, H. *Phys. Rev. B* **1999**, *59*, 10970.
- (100) Ray, U.; Jarold, M. F.; Bower, J. E.; Kraus, J. S. *Chem. Phys. Lett.* **1989**, *159*, 221.
- (101) Terasaki, A.; Minemoto, S.; Kondow, T. *J. Chem. Phys.* **2002**, *117*, 7520.
- (102) Tono, K.; Terasaki, A.; Ohta, T.; Kondow, T. *J. Chem. Phys.* **2005**, *123*, 174314.
- (103) Jarrold, M. F.; Illies, A. J.; Bowers, M. T. *J. Am. Chem. Soc.* **1985**, *107*, 7339.
- (104) Jarrold, M. F. Transition metal clusters: Physical properties. In *Clusters of atoms and molecules I*; Haberland, H., Ed.; Springer-Verlag: Berlin, 1995; p 315.
- (105) Russon, L. M.; Heidecke, S. A.; Birke, M. K.; Conceicao, J.; Morse, M. D.; Armentrout, P. B. *J. Chem. Phys.* **1994**, *100*, 4747.
- (106) Terasaki, A.; Matsushita, A.; Tono, K.; Yadav, R. T.; Briere, T. M.; Kondow, T. *J. Chem. Phys.* **2001**, *114*, 9367.
- (107) Terasaki, A.; Briere, T. M.; Kulawik, M.; Minemoto, S.; Tono, K.; Matsushita, A.; Kondow, T. *J. Chem. Phys.* **2003**, *118*, 2180.
- (108) For example, Kittel, C. *Introduction to Solid State Physics*, 5th ed.; John Wiley: New York, 1976.
- (109) Baumann, C. A.; Van Zee, R. J.; Bhat, S. V.; Weltner, W., Jr. *J. Chem. Phys.* **1983**, *78*, 190.
- (110) Bauschlicher, C. W., Jr. *Chem. Phys. Lett.* **1989**, *156*, 95.
- (111) Van Zee, R. J.; Weltner, W., Jr. *J. Chem. Phys.* **1988**, *89*, 4444.
- (112) Van Zee, R. J.; Baumann, C. A.; Weltner, W., Jr. *J. Chem. Phys.* **1981**, *74*, 6977.
- (113) Briere, T. M.; Terasaki, A.; Kondow, T. Unpublished data.
- (114) Knickelbein, M. B. *Phys. Rev. Lett.* **2001**, *86*, 5255.
- (115) Knickelbein, M. B. *Phys. Rev. B* **2004**, *70*, 014424.
- (116) Fujima, N.; Yamaguchi, T. *J. Phys. Soc. Jpn.* **1995**, *64*, 1251.
- (117) Nayak, S. K.; Jena, P. *Chem. Phys. Lett.* **1998**, *289*, 473.
- (118) Nayak, S. K.; Rao, B. K.; Jena, P. *J. Phys. Condens. Matter* **1998**, *10*, 10863.
- (119) Pederson, M. R.; Reuse, F.; Khanna, S. N. *Phys. Rev. B* **1998**, *58*, 5632.
- (120) Briere, T. M.; Sluiter, M. H. F.; Kumar, V.; Kawazoe, Y. *Phys. Rev. B* **2002**, *66*, 064412.
- (121) Bobadova-Parvanova, P.; Jackson, K. A.; Srinivas, S.; Horoi, M. *Phys. Rev. A* **2003**, *67*, 061202(R).
- (122) Khanna, S. N.; Rao, B. K.; Jena, P.; Knickelbein, M. *Chem. Phys. Lett.* **2003**, *378*, 374.
- (123) Jones, N. O.; Khanna, S. N.; Baruah, T.; Pederson, M. R. *Phys. Rev. B* **2004**, *70*, 045416.
- (124) Morisato, T.; Khanna, S. N.; Kawazoe, Y. *Phys. Rev. B* **2005**, *72*, 014435.
- (125) Gutsev, G. L.; Mochena, M. D.; Bauschlicher, C. W., Jr. *J. Phys. Chem. A* **2006**, *110*, 9758.
- (126) Majima, T.; Tono, K.; Terasaki, A.; Kawazoe, Y.; Kondow, T. *Eur. Phys. J. D*, in press.
- (127) Gspann, J.; Krieg, G. *J. Chem. Phys.* **1974**, *61*, 4037.
- (128) Holland, R. J.; Xu, G.-Q.; Levkoff, J.; Robertson, A., Jr.; Bernasek, S. L. *J. Chem. Phys.* **1988**, *88*, 7952.
- (129) Vach, H.; De Martino, A.; Benslimane, M.; Châtelet, M.; Pradère, F. *J. Chem. Phys.* **1994**, *100*, 8526.
- (130) Vach, H.; Benslimane, M.; Châtelet, M.; De Martino, A.; Pradère, F. *J. Chem. Phys.* **1995**, *103*, 1972.
- (131) Leidenfrost, J. G. *De Aquae Communis Nonnullis Qualitatibus Tractatus (A tract about some qualities of common water)*, Duisburg on Rhine, 1756. An English translation: *On the fixation of water in diverse fire*, *Int. J. Heat Mass Transfer.* **1966**, *9*, 1153. Translated by C. Wares. Introduction by K. J. Bell.
- (132) Gottfried, B. S.; Lee, C. J.; Bell, K. J. *Int. J. Heat Mass Transfer* **1966**, *9*, 1167.
- (133) Cleveland, C. L.; Landman, U. *Science* **1992**, *257*, 355.
- (134) Even, U.; Schek, I.; Jortner, J. *Chem. Phys. Lett.* **1993**, *202*, 303.
- (135) Schek, I.; Jortner, J. *J. Chem. Phys.* **1996**, *104*, 4337.
- (136) Raz, T.; Even, U.; Levine, R. D. *J. Chem. Phys.* **1995**, *103*, 5394.
- (137) Hendell, E.; Even, U.; Raz, T.; Levine, R. D. *Phys. Rev. Lett.* **1995**, *75*, 2670.
- (138) Christen, W.; Even, U.; Raz, T.; Levine, R. D. *Int. J. Mass Spectrom. Ion Processes* **1998**, *174*, 35.
- (139) Even, U.; Kondow, T.; Levine, R. D.; Raz, T. *Comments Atom. Mol. Phys. Comments Mod. Phys.* **1999**, *1*, Part D, 1.
- (140) Raz, T.; Levine, R. D. *J. Phys. Chem.* **1995**, *99*, 7495.
- (141) Ceyer, S. T. *Science* **1990**, *249*, 133.
- (142) Tsukuda, T.; Yasumatsu, H.; Sugai, T.; Terasaki, A.; Nagata, T.; Kondow, T. *J. Phys. Chem.* **1995**, *99*, 6367.
- (143) Terasaki, A.; Tsukuda, T.; Yasumatsu, H.; Sugai, T.; Kondow, T. *J. Chem. Phys.* **1996**, *104*, 1387.
- (144) Yasumatsu, H.; Koizumi, S.; Terasaki, A.; Kondow, T. *J. Chem. Phys.* **1996**, *105*, 9509.
- (145) Terasaki, A.; Yasumatsu, H.; Kalmbach, U.; Fukuda, Y.; Koizumi, S.; Yamaguchi, H.; Kondow, T. In *Structures and Dynamics of Clusters*; Kondow, T., Kaya, K., Terasaki, A., Eds.; Universal Academy Press, Inc.: Tokyo, 1996; p 273.
- (146) Terasaki, A.; Yasumatsu, H.; Fukuda, Y.; Yamaguchi, H.; Kondow, T. *RIKEN Rev.* **1998**, *17*, 31.
- (147) Nakajima, A.; Kishi, T.; Sugioka, T.; Sone, Y.; Kaya, K. *Chem. Phys. Lett.* **1991**, *177*, 297.
- (148) Leskiw, B. D.; Castleman, A. W., Jr. *Chem. Phys. Lett.* **2000**, *316*, 31.
- (149) Ashman, C.; Khanna, S. N.; Pederson, M. R. *Chem. Phys. Lett.* **2000**, *324*, 137.
- (150) Ashman, C.; Khanna, S. N.; Pederson, M. R.; Kortus, J. *Phys. Rev. B* **2000**, *62*, 16956.
- (151) Marton, D.; Boyd, K. J.; Lytle, T.; Rabalais, J. W. *Phys. Rev. B* **1993**, *48*, 6757.
- (152) St. John, P. M.; Whetten, R. L. *Chem. Phys. Lett.* **1992**, *196*, 330.
- (153) For example, Landau, L. D.; Lifshitz, E. M. *Statistical Physics, Part I*, 3rd ed.; Pergamon: Oxford, U.K., 1980.
- (154) Hettich, R. L. *J. Am. Chem. Soc.* **1989**, *111*, 8582.
- (155) Terasaki, A.; Yamaguchi, H.; Yasumatsu, H.; Kondow, T. *Chem. Phys. Lett.* **1996**, *262*, 269.
- (156) Terasaki, A.; Tsukuda, T.; Yasumatsu, H.; Sugai, T.; Kondow, T. *Surf. Rev. Lett.* **1996**, *3*, 591.
- (157) Liu, Y.; Zhang, Q.-L.; Tittel, F. K.; Curl, R. F.; Smalley, R. E. *J. Chem. Phys.* **1986**, *85*, 7434.
- (158) Bloomfield, L. A.; Freeman, R. R.; Brown, W. L. *Phys. Rev. Lett.* **1985**, *54*, 2246.
- (159) Zhang, Q.-L.; Liu, Y.; Curl, R. F.; Tittel, F. K.; Smalley, R. E. *J. Chem. Phys.* **1988**, *88*, 1670.
- (160) Jarrold, M. F.; Bower, J. E. *J. Phys. Chem.* **1988**, *92*, 5702.
- (161) Tai, Y.; Murakami, J.; Majumder, C.; Kumar, V.; Mizuseki, H.; Kawazoe, Y. *Eur. Phys. J. D* **2003**, *24*, 295.
- (162) Saunders, W. A.; Fayet, P.; Wöste, L. *Phys. Rev. A* **1989**, *39*, 4400.
- (163) Jarrold, M. F.; Bower, J. E.; Kraus, J. S. *J. Chem. Phys.* **1987**, *86*, 3876.
- (164) Hanley, L.; Ruatta, S. A.; Anderson, S. L. *J. Chem. Phys.* **1987**, *87*, 260.
- (165) Krückeberg, S.; Dietrich, G.; Lützenkirchen, K.; Schweikhard, L.; Walther, C.; Ziegler, J. *Int. J. Mass Spectrom. Ion Processes* **1996**, *155*, 141.
- (166) Tai, Y.; Yamaguchi, W.; Maruyama, Y.; Yoshimura, K.; Murakami, J. *J. Chem. Phys.* **2000**, *113*, 3808.
- (167) Yasumatsu, H.; Tsukuda, T.; Sugai, T.; Terasaki, A.; Nagata, T.; Kondow, T. *Surf. Rev. Lett.* **1996**, *3*, 901.
- (168) Yasumatsu, H.; Terasaki, A.; Kondow, T. *J. Chem. Phys.* **1997**, *106*, 3806.
- (169) Amar, F. G.; Perera, L. Z. *Phys. D* **1991**, *20*, 173.
- (170) Ray, D.; Levinger, N. E.; Papanikolas, J. M.; Lineberger, W. C. *J. Chem. Phys.* **1989**, *91*, 6533.
- (171) Papanikolas, J. M.; Gord, J. R.; Levinger, N. E.; Ray, D.; Vorsa, V.; Lineberger, W. C. *J. Phys. Chem.* **1991**, *95*, 8028.

- (172) Yasumatsu, H.; Kalmbach, U.; Koizumi, S.; Terasaki, A.; Kondow, T. *Z. Phys. D* **1997**, *40*, 51.
- (173) Yasumatsu, H.; Koizumi, S.; Terasaki, A.; Kondow, T. *J. Chem. Phys.* **1996**, *105*, 9509.
- (174) Yasumatsu, H.; Koizumi, S.; Terasaki, A.; Kondow, T. *J. Phys. Chem. A* **1998**, *102*, 9581.
- (175) Morgner, N.; Barth, H.-D.; Brutschy, B. *Aust. J. Chem.* **2006**, *59*, 109.
- (176) Kohno, J.; Toyama, N.; Kondow, T. *Chem. Phys. Lett.* **2006**, *420*, 146.
- (177) Kadanoff, L. P. *Phys. Today* **2001**, August, 34.
- (178) Terasaki, A.; Kondow, T. Unpublished data.
- (179) O'Keefe, A.; Deacon, D. A. G. *Rev. Sci. Instrum.* **1988**, *59*, 2544.
- (180) Terasaki, A.; Egashira, K.; Kondow, T. *J. Opt. Soc. Am. B* **2005**, *22*, 675.
- (181) O'Keefe, A.; Scherer, J. J.; Cooksy, A. L.; Sheeks, R.; Heath, J.; Saykally, R. J. *Chem. Phys. Lett.* **1990**, *172*, 215.
- (182) Scherer, J. J.; Paul, J. B.; O'Keefe, A.; Saykally, R. J. *Chem. Rev.* **1997**, *97*, 25.
- (183) Kraus, D.; Saykally, R. J.; Bondybey, V. E. *Chem. Phys.* **1999**, *247*, 431.
- (184) Labazan, I.; Milošević, S. *Phys. Rev. A* **2003**, *68*, 032901.
- (185) Terasaki, A.; Majima, T.; Kondow, T. Unpublished data.
- (186) Engeln, R.; von Helden, G.; van Rooij, A. J. A.; Meijer, G. *J. Chem. Phys.* **1999**, *110*, 2732.
- (187) Aarts, I. M. P.; Hoex, B.; Smets, A. H. M.; Engeln, R.; Kessels, W. M. M.; van de Sanden, M. C. M. *Appl. Phys. Lett.* **2004**, *84*, 3079.
- (188) Antonietti, J.-M.; Michalski, M.; Heiz, U.; Jones, H.; Lim, K. H.; Rösch, N.; Del Vitto, A.; Pacchioni, G. *Phys. Rev. Lett.* **2005**, *94*, 213402.
- (189) Charvat, A.; Stasicki, B.; Abel, B. *J. Phys. Chem. A* **2006**, *110*, 3297.
- (190) Toyama, N.; Kohno, J.; Kondow, T. *Chem. Phys. Lett.* **2006**, *420*, 77.
- (191) Kohno, J.; Mafuné, F.; Kondow, T. *Bull. Chem. Soc. Jpn.* **2005**, *78*, 957.
- (192) Toyama, N.; Kohno, J.; Mafuné, F.; Kondow, T. *Chem. Phys. Lett.* **2006**, *419*, 369.
- (193) Kohno, J.; Toyama, N.; Buntine, M. A.; Mafuné, F.; Kondow, T. *Chem. Phys. Lett.* **2006**, *420*, 18.
- (194) Schmidt, M.; Kusche, R.; von Issendorff, B.; Haberland, H. *Nature (London)* **1998**, *393*, 238.
- (195) Frenzel, U.; Roggenkamp, A.; Kreisle, D. *Chem. Phys. Lett.* **1995**, *240*, 109.
- (196) Frenzel, U.; Kalmbach, U.; Kreisle, D.; Recknagel, E. *Surf. Rev. Lett.* **1996**, *3*, 505.
- (197) Mitzner, R.; Campbell, E. E. B. *Surf. Rev. Lett.* **1996**, *3*, 759.
- (198) Walther, C.; Dietrich, G.; Dostal, W.; Hansen, K.; Krückeberg, S.; Lützenkirchen, K.; Schweikhard, L. *Phys. Rev. Lett.* **1999**, *83*, 3816.
- (199) Levine, R. D. Private communication.